TAMPERE UNIVERSITY OF TECHNOLOGY
Department of Biomedical Engineering

Adeola Olubamiji

The Influence of Filtration, Tube Current and Number of Projections on CBCT Image quality

Master of Science Thesis

Subject and Supervisors approved by the Department Council on June 6, 2011.
Supervisors: Professor Jari Hyttinen
Jan Wolff (DDS, PhD)

ABSTRACT

TAMPERE UNIVERSITY OF TECHNOLOGY
Master's Degree Programme in Biomedical Engineering
ADEOLA OLUBAMIJI: The Influence of Filtration, Tube Current and Number of Projections on CBCT Image Quality.
Masters of Science Thesis, 69 pages, 3 Appendices
June, 2011
Examiners: Professor Jari Hyttinen
Docent Prasun Dastidar
Major Subject: Medical Physics
Funding and Experiments: Medical Imaging Centre, Department of Radiology, Tampere University Hospital, Tampere, Finland.
Keywords**:** Radiology, temporal bone, X-ray, computed tomography, filters, Image quality, Cone Beam CT (CBCT), Cadaver head, temporal bone image, Aluminum, Copper, field of view (FOV), mAs, filters, number of projections, MATLAB.

As cone-beam computed tomography (CBCT) is becoming popular in temporal bone imaging, there is a pressing need to improve the quality of images rendered by this device in temporal bone imaging. This prospective cadaver study aims at evaluating the image quality and assessing the changes that result when three different filter combinations, variation in the number of projections, and tube current are used in CBCT temporal bone imaging. The image acquisition was carried out using three filter combinations, Cu-Al, Cu-Cu and Al-Al, with varying thickness and the number of projections was changed from the standard 100% to 150%. Additionally, 8 mA and 12.5 mA were used in all cases. The quality of the acquired images was then qualitatively (visually) and quantitatively (noise analysis) assessed. The visual assessment was carried out by two radiologists with over 20 years' experience in the field of diagnostic radiology and the noise analysis (standard deviation), an algorithm-based assessment, was done in MATLAB user interface.
The results showed that Copper and Aluminum (Cu-Al) filters offered the best image quality when compared with the Cu-Cu (factory-fitted) and Al-Al filter combinations in both visual and algorithm-based assessments. From the results, it was also demonstrated that increasing the number of projections from the standard 100% number of projections to 150% offered a better characterization of the complex temporal bone anatomy in both visual and noise analysis assessments. Finally, changes in the tube current from 8 mA to 12.5 mA resulted in a minimal change of the image quality when visually assessed. However, the effects of the tube current variations increased when the algorithm-based noise analysis was carried out.

In conclusion, variations in the material property of the filter, effective filter inter-positioning, and variations in the number of projections optimize the image quality in CBCT temporal bone imaging.

PREFACE

This thesis is based on the studies conducted from December 2010 to September 2011 at the Medical Imaging Centre, Department of Radiology, Tampere University Hospital, Tampere, Finland in collaboration with the Department of Biomedical Engineering, Tampere University of Technology, Tampere, Finland.

Firstly, I would like to express my gratitude to God Almighty for his unfailing love and for being there for me always. Additionally, I would like to express my sincere gratitude to my supervisor, teacher and motivator, Professor Jari Hyttinen for his immense teachings and all the research opportunities he offered me during my study years at this university. I want to also specially thank Professor Hannu Eskola for his quality teachings in the past years in the field of medical physics as they all formed the basis of my knowledge for this thesis.

Also, I want to specially thank my group of supervisors at the Medical Imaging Centre, Department of Radiology, Tampere University Hospital, Tampere, Finland: Jan Wolff (DDS, PhD), Jorma Jarnstedt (DDS) and Prasun Dastidar (MD PhD) for their full support, time, funding, valuable experts' advice and mentorship. Without your helpful and cooperative attitude towards the study, the results of this thesis would not exist. I would also like to thank Soredex, Helsinki, Finland for providing the custom-made filters and allowing us to use them on their device.

Furthermore, I want to specially thank Mr Peter Heath, my research communication educator, for his time, efforts, teaching, proofreading of this thesis and for laying a concrete foundation for future research for me. I also want to express my heart-felt gratitude to my teachers and tutors: Katrina Wendel (PhD), Markus Hannula (MSc), Ayodeji Olatunbosun (MSc), Olanrewaju Olotu (Msc), Nathaniel Narra (MSc), Tomas Cervinka (PhD), and Ayodeji Akinsemolu (MSc) for their advices, valuable tips and support during the writing of this thesis and my entire study period at this university. Finally, I want my express my greatest thanks to my friends: Ogunyale Oladayo, Carl Magnus, Seyoum Nerisho, Gabriel Nketiah, Oluwasanmi Aderinola and the Olubamiji family for their love, encouragement and support.
Tampere, September 2011

Adeola Olubamiji

0466219977

TABLE OF CONTENTS

LIST OF ABBREVIATIONS AND SYMBOLS

ALARA	As low as reasonably achievable
CBCT	Cone beam computed tomography
CNR	Contrast-to-noise ratio
CsI	Cesium iodide
CT	Computed tomography
CTDI	Computed tomography dose index
D	Absorbed dose
E	Effective dose
EC	European Commission
FOV	Field of view
FPD	Flat panel detector
Gy	Gray
H_T	Equivalent dose
HU	Hounsfield unit
HVL	Half value layer
ICRP	International Commission on Radiological Protection
IID	Image intensifier detector
kerma	Kinetic energy released per unit mass
Kv(p)	Kilovolt (peak)
LFS	Line spread function
mA	Milliampere
mAs	Milliampere seconds
Ms	Millisecond
MSE	Mean square error
MPR	Multiplanar reformation
MRI	Magnetic resonance imaging
MTF	Modulation transfer function
MDCT	Multidetector computed tomography

PSP	Photostimulable phosphor plate
PSF	Point spread function
PSNR	Peak-signal-to-noise ratio
ROI	Region of interest
SNR	Signal-to-noise ratio
STUK	Radiation and Nuclear Safety Authority (Säteilyturvakeskus)
Sv	Sievert
W_R	Radiation weighting factor
W_T	Tissue weighting factor
2D	Two-dimensional
3D	Three-dimensional
$\sum$	Summation

1. INTRODUCTION

As the anatomy of temporal bone is complex and contains many small but clinically important bones, air spaces, and varieties of soft tissues, temporal bone imaging is one of the most challenging protocols in diagnostic imaging [5; 22; 23]. The chosen imaging method selected for surgical planning, pre- and post-operative follow up, interoperative guidance, and other diagnoses of ear related disorders must be able to reveal even the smallest anatomical details in the temporal bone. This is because very small damage in this area often results in significant problems if the patient does not receive proper care. As a result, high resolution images that can reveal the complex anatomical nature of temporal bone are of major importance when temporal bone diagnosis is required [5; 15; 21; 22; 44; 56; 57].

1.1 Objectives of the thesis

The objective of this thesis is to comparatively analyze the changes in image quality that arise in the temporal bone area using different filter combinations, number of projections and milliamperage (tube current) on the SCANORA 3D, cone-beam 3D imaging system (CBCT). The findings of this thesis will provide understanding about the effects of variations in the material property of the filter, and variations in the number of projections and tube current on image quality in CBCT temporal bone imaging. This research will also underline the need for further research on the effects of exposure parameters and filtration to optimize image quality in CBCT.

At present, multi-detector computed tomography (MDCT) of high enough resolution is used as a standard method for temporal bone imaging. High-resolution images of the temporal bone are obtained in most cases using a 64-slice MDCT imaging device [5; 15; 22; 44]. The main advantages of MDCT for temporal bone imaging are shorter acquisition times, a decrease in tube current load and better spatial resolution [44; 51; 55]. The short acquisition time is an advantage especially when dealing with younger

patients and patients in severe pain that often need sedatives to calm them down for appropriate image acquisition. The ability of MDCT to obtain images of both temporal bones in one scan is another reason why MDCT is effective for imaging the temporal bone [5; 22]. The wide difference in temporal bone structures and the ability to obtain the images of both temporal bones simultaneously is one of the reasons why MDCT excels in this area. Despite the advantages of this method, MDCT examinations are known for the high radiation dose delivered to patients. MDCT delivers an even higher radiation dose when compared with single detector CT scanners [22; 56]. Additionally, temporal bone imaging requires high quality images that in most cases require high resolution scanning; hence a higher radiation dose is required [5; 15; 22; 56]. Furthermore, for follow-up and interoperative scanning, the dose cumulatively increases when MDCT is used and this may pose huge challenges for the use of MDCT in such case [8; 44; 55].

Magnetic resonance imaging (MRI) of 1.5 Tesla (T) strength is another method used in inner ear imaging. High resolution MR imaging has an advantage over all types of CT imaging of the temporal bone as it gives a better soft tissue and fluid-filled characterization [5; 22; 57]. MRI scanning requires no radiation for its acquisition and it is completely safe for multiple usage and diagnosis follow-up [44: 56]. Despite several advantages, the major limitations of this method are the lack of bony details and the signal void experienced during the application of the radiofrequency pulse [22; 56; 57]. This is due to the lack of water containing material and mobile protons in the dense cortical bones. Another major disadvantage of using this method in temporal bone imagining is the very high cost of the examination and the sedation needed for younger patients or patients in severe pain [22]. In addition, this method cannot be used for interoperative imaging were metal objects are needed for the operations as the superconducting magnets will attract the metals. Also, for patients who are allergic to certain contrast agents, another type of contrast agent that may cost more is required. In summary, the use of MRI in temporal bone imaging is dependent on the area to be visualized, age [57], the pathology involved and its severity level. MRI may serve as a complementary method when CT is used [22; 55; 56; 57; 63].

The use of cone beam computed tomography (CBCT) imaging has progressed rapidly in temporal bone imaging. This has inevitably led to many new questions concerning its exact applicability, in terms of image quality, when compared with multi detector computed tomography (MDCT) in temporal bone imaging. CBCT provides digital, volumetric and interactive images that can be used for diagnostic and surgical planning purposes [10; 38; 39; 55]. It was introduced in 1997, and since then, it has been increasingly used for image guidance, dental radiology, and angiography. The frequent use of CBCT temporal bone diagnosis is based on its good characterization of bony structures with a radiation dose low enough to allow repeated imaging [30; 47; 54; 63]. As the radiation dose offered by CBCT is often lower than what is used in multi-slice computed tomography (MSCT) or MDCT [14], when the focus is on limited field of view (FOV), the use of CBCT in temporal bone imaging may be considered as a good option. This is because CBCT follows the "As Low As Reasonably Achievable" (ALARA) principle concerned with the use of lower radiation dose in diagnostic imaging [22; 28; 30]. However, an accepted ratio between exposure and image quality must be reached in order to use the ALARA principle as no exposure to X-rays is completely safe or free of risk (EC 2004) and image quality must not be compromised [30; 47; 54; 63]. This hypothesis then raised the question whether CBCT could be used as an alternative to MDCT for temporal bone imaging even when repeated investigation from a small portion of an anatomy is required. Furthermore, CBCT differs from conventional CT in its smaller size, shorter acquisition time, lower cost, limited field of view and the lower radiation dose, and convenience in patient positioning [17; 36; 50; 52].

However, the presence of artifacts, noise, less uniformity, and low contrast resolution caused by the image acquisition and reconstruction techniques have been shown to have a negative effect on CBCT image quality [14; 25; 27; 29]. Consequently, the image quality offered by CBCT in temporal bone imaging is often lower when compared with MDCT for this purpose. This hinders the effective analysis of the complex temporal bone anatomy from the acquired images [14; 51; 54; 55; 57]. In order to tackle this problem, this thesis focuses on one of the possible solutions: optimizing the image quality through the use of different filtration possibilities in CBCT imaging. In most CBCT devices, the filters are often made of aluminum or copper [11; 29; 52]. The filtration process does not only lead to the removal of low energy X-rays, but it also

reduces the exposure of the skin to radiation [11; 29; 52]. The use of filter materials with atomic number (Z) higher than that of aluminum (Al) are known to enhance image quality. An example is the use of copper (Cu) or tin (Sn) that allows greater attenuation of low energy photons [11; 25; 27; 29; 35; 52].

A considerable amount of literature has been published on temporal bone imaging, effects of filtration, and the use of CBCT. Table 1 presents some of the pioneering studies related to this work.

Table 1: Pioneer study in effects of filtration, number of projections and tube current in CT imaging.

Author	Study question	Data and modality used	Results and conclusions
Milton Costa et al. (2009)	Effect of additional filtration on radiation doses and image quality in videofluoroscopic studies.	An ionization chamber coupled with an electrometer was added to X-ray tube to measure the kerma area product with 65 kV and 0.7 mA technique, without and with additional filtration.	Additional aluminum and copper filters interposition, especially when associated, results in improved image quality with expressive reduction in the required radiation doses [9].
Dalchow et al. (2006)	Digital volume tomography: Radiologic examinations of the temporal bone.	Twenty-five patients with a history of a progressive hearing loss were imaged with digital volume tomography (DVT), an extension of panoramic tomography [10].	In conclusion, they stated that DVT is an excellent technique to examine the middle ear cleft and inner ear with minimum radiation dose [10].
Sohaib et al. (2001)	The effect of decreasing mAs on image quality and patient dose in sinus CT.	Forty consecutive patients undergoing paranasal sinus CT. Ten patients were scanned at 200 mAs, 150 mAs, 100	No significant difference was shown between any of the four groups in terms of image quality according to the scoring

		mAs and 50 mAs, respectively. Images were received by two observers who were not aware of the mAs settings.	system used in this study [54].
Palomo et al. (2006)	Influence of mA settings and a copper filter in CBCT image resolution.	A C-Phantom that contains 9 sets of metal lines submerged in water was imaged using CBCT to test the image resolution at 2 mA, 5 mA, 10 mA, and 15 mA.	They concluded that the images with the higher milliamperage and a copper filter showed the best resolution [41].
Devito et al. (2006)	Copper filter for dental radiology: evaluation of radiographic contrast.	Aluminum wedge was imaged using a dental X-ray machine with alternative copper filtration.	It was concluded that the use of copper filter yielded better contrast but required longer exposure times. It reduces the air-kerma rate and results in higher contrast values than those obtained with an aluminum filter [11].
Sakata et al. (2007)	Optimization of TACT imaging protocols for in situ visualization of cochlear electrode arrays in cat temporal bones.	Cadaveric cat temporal bones were scanned with Tuned Aperture Computed Tomography (TACT).	The quality of the resulting images, evaluated as a function of image contrast, improved with a larger number of basis images in the reconstruction. Wider projection angles also improved image

			detail in addition to generating thinner slices [50].

1.2 Overview of Research Methodology

This study was carried out at the Medical Imaging Centre, Department of Radiology, Tampere University Hospital, Tampere, Finland. It is a major cadaver study that included the sinus and temporal bone assessment. My part of the study included the image acquisition and image analysis of the temporal bone images. The study assessed the effect of filtration, varying exposure parameters, and tube current on CBCT image quality. An overview of the structure of the study is presented in Figure 1.1.

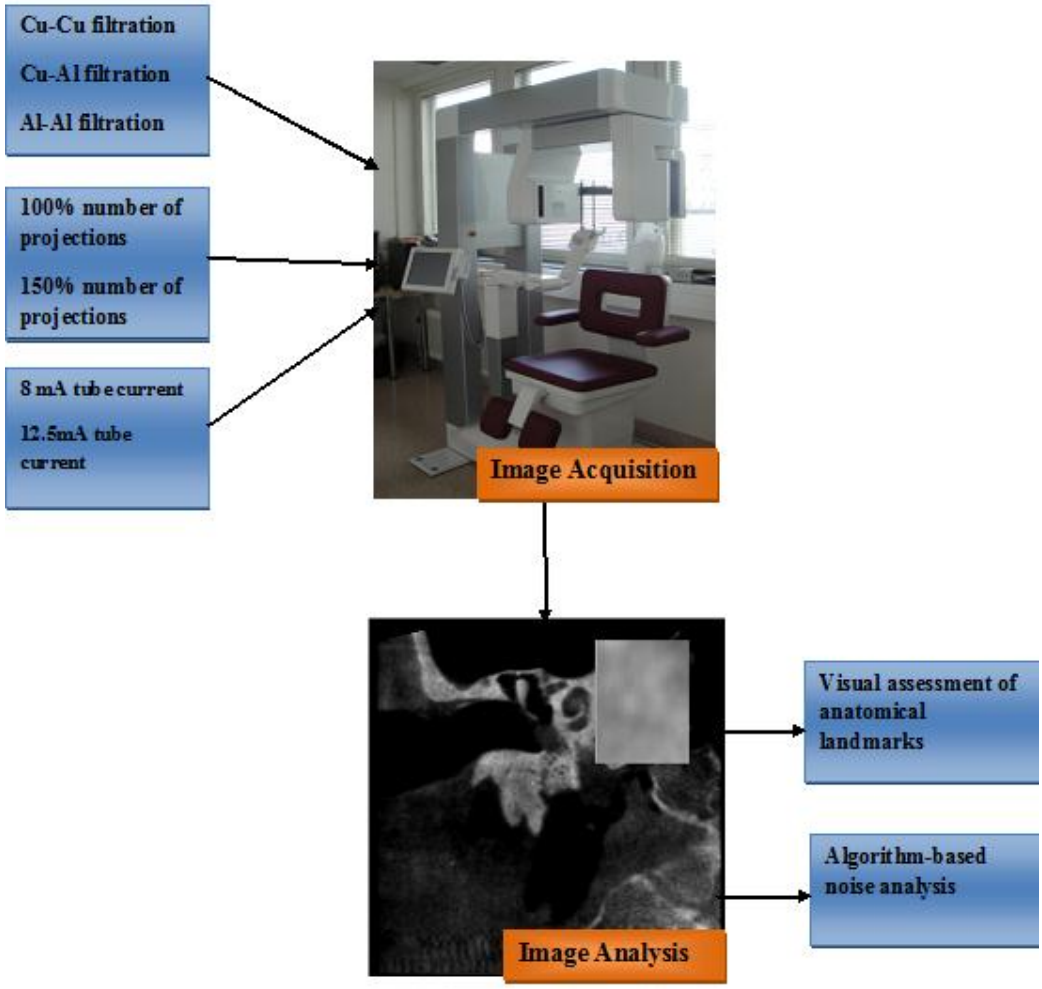

Figure 1.1: An overview of the structure of the study.

2. THEORETICAL BACKGROUND

This chapter reviews the theoretical background of radiography, the generations of CT scanners, and a brief description of temporal bone imaging.

Radiography is the use of penetrating X-rays to generate images of an optically opaque, non-uniform object such as the human body [12; 34; 38; 39; 55]. In conventional X-ray imaging, an object is irradiated by photons generated from an X-ray source and the transmitted photons are registered on a photographic and optically reflective layer (detector). One of the major setbacks in radiology is the reduction of the 3D patient anatomy to a 2D projection image [34]. In order to further develop radiographic imaging, computed tomography originally called the "EMI" scan (research funded by the EMI music group) evolved from radiographic imaging. Computed tomography (CT) is a non-invasive, diagnostic technique in which a large series of cross-sectional, 2D X-ray images or tomographic slices are used to generate 3D images of the internals of an object [12; 19; 34; 55]. It produces a high-contrast image with uniform magnification with well-defined image layer free of blurring and gives the possibility to reconstruct images in three-dimension.

Furthermore, the invention of the CT scanner is said to be the most important development in radiology since the discovery of X-rays by Konrad Rontgen [12; 34]. CT technology was first described in 1917 by Radon, an Austrian mathematician who wrote his thesis on this topic. However, the effect of his work was not recognized until over 50 years after the publication was released [34]. In 1979, a British Engineer G.N. Hounsfield and an American theoretical physicist A.M. Cormack were jointly awarded the Nobel Prize in medicine for their invention of CT [12; 19; 34]. Two major methods can be used in CT scanning: sequential scanning and spiral scanning [19]. In sequential CT, the image produced is cross-sectional and scanning is achieved by capturing transverse slices of the body from different orientations. The capturing occurs as the source and the detector rotate round the stationary patient at 360^0. Conversely, in spiral CT, the patient table is moved through the scan field in a z-direction while the gantry

head performs several 360^0 rotations in the same direction. This forms a spiral-like pattern around the body and generates a data volume from the superposition of the free images generated from the data [12; 19; 34].

2.1 Generations of CT Scanners

Since Hounsfield's invention of the EMI scanner, several sets of CT acquisition geometries, x-ray sources, and detectors have been developed for visualization, diagnostic, and therapeutic purposes. These are referred to as generations [38, 56]. The first through fourth-generation CT systems used X-rays in single plane and are explained below.

Early Generations of CT scanners

The first generation of CT scanners consisted of an X-ray source and a single detector. The image was acquired by directing a parallel, pencil beam from the x-ray source through the object to a single detector along a straight line in the scan plane. The procedure was repeated for the next projection and a number of angular orientations obtained by rotating the frame by 1-degree intervals between translations to acquire 180 projections [12; 19; 34]. The second-generation of CT scanners used similar translation-rotation procedure as used in the first generation. Moreover, it replaced the pencil beam and the single detector by a fan beam and linear array of multiple detectors respectively. This provides enhanced data acquisition with improved image quality and shorter scan time compared with the first generation scanner [12; 19; 34].

In the third-generation scanner, the number of detectors was increased, forming an arc-shaped array of detectors. The angle of the fan beam was also increased with a field of view (FOV) wide enough to totally encompass the slice of interest. The source-detector combination rotates around the object at very high speed, often completing a full 360^o rotation in less than one second. In the first through third generation scanners, the motion between the object being scanned and the source-detector pair is relative, and can be accomplished either by keeping the object stationary and moving the source-detector pair, as is done in medical CT systems, or vice versa as is more common in industrial systems [12; 14; 34; 52; 50]. The fourth generation design consists of a stationary, complete ring of detectors and a single X-ray source that orbits around the object being scanned. The major drawback of the fourth generation of CT scanners is

the very high cost of the detector array and this has propelled the development of CT scanners from fan beam to cone beam geometry [12; 34; 38].

E-beam generation of CT scanners

Electron-beam computerized tomography (EBCT), also known as ultrafast and sensitive CT, was designed to diagnose the calcium build-up in the arteries of the heart [34]. It was developed in 1996 at the Lucile Salter Packard Children's Hospital, Stanford, California [30]. Since the heart cannot be stopped during imaging, EBCT technology allows easier and better visualization of the pumping heart than conventional CT technology. A combination of lung function and breathing cycle markers trigger the e-beam scanner at specific breath levels to perform a complete cycle of movement with each heart beat [34].

E-beam CT scanners use an electron gun and a circular ring of detector. The set-up possesses smaller source-detector separation and short electron path which results in an ultrafast scanning. The scanning method is ten-times faster as there are no mechanical moving parts and a complete dataset for image reconstruction is generated in less than 100 ms, thus, reducing the need for sedative agents and lowers patient dose per scan. The electron gun, which has no mechanical spin, emits X-rays after the electrons hit the target. The target is a stationary X-ray source point and the electron beam is swept rapidly across the stationary target electromagnetically to generate X-ray from the moving focal spot. After the production of X-rays, the photons traverse the object, forming an image on the stationary array of fast X-rays detectors [30; 34].

2.2 Principles of Cone-beam Computed Tomography and Temporal bone imaging

CBCT is a recent volumetric imaging method introduced in 1997 and developed initially for angiography [38; 39]. In recent years, it has been increasingly used in applications such as radiotherapy guidance [12], mammography [51], and maxillofacial diagnosis including implant site imaging, treatment planning, craniofacial surgery, and dentoalveolar applications [25; 55; 60]. A collimated cone shaped beam is used instead of a fan beam, and a planar grid replaces the linear series of detectors that captures

several 2D projection images and constructs them into 3D images mathematically. This allows for much faster data acquisition, as the data required for multiple slices can be acquired in one rotation. However, CBCT is also computationally more intensive, prone to distortion, and in many cases provides lower-resolution images [25; 34; 50]. Interestingly, it has recently emerged as a potentially low dose cross-sectional means of visualizing bony structures in the temporal bone area of the head [14].

CBCT technology uses a rotating gantry head that contains an X-ray source and a detector [51]. The tightly collimated, cone-shaped, pulsed or continuous X-ray flux emerging from the X-ray tube irradiates the object. In CBCT, the cylindrical FOV restricts the X-ray beam and may be selected to suit the examination. The image of the traversed object is then captured by a flat panel detector behind the object depending on the chosen FOV. A sequence of 2D projection images (from 150 to more than 600) of the chosen FOV are recorded with a 2D detector from a single 180 to 360 degree gantry rotation. These projection images are then reconstructed into a 3D image mathematically [12; 34; 55]. This acquisition method also differs from what is offered by conventional MDCT where each slice is acquired in a separate scan and a separate 2D reconstruction is done for each slice. For this reason, CBCT is a faster method with optimized photon use, and computationally more intensive [19; 51]. On the other hand, the positioning of the field of view (FOV) in CBCT, which uses a single projection, is prone to error that reduces image contrast and also increases the noise level in the images [55]. This is due to the summing of attenuation structures in the depth direction and the substantially high scatter of the beam [12; 19; 34; 38].

Data acquisition modes of CBCT devices differ from one manufacturer to another and from medical CT (MDCT or MSCT) systems. The SCANORA 3D cone beam 3D imaging system (Soredex, Tuusula, Finland) used in this study allows the patient to sit comfortably and fixes the patient's head to the head support using a head strap. This allows a precise image acquisition (Fig 2.1).

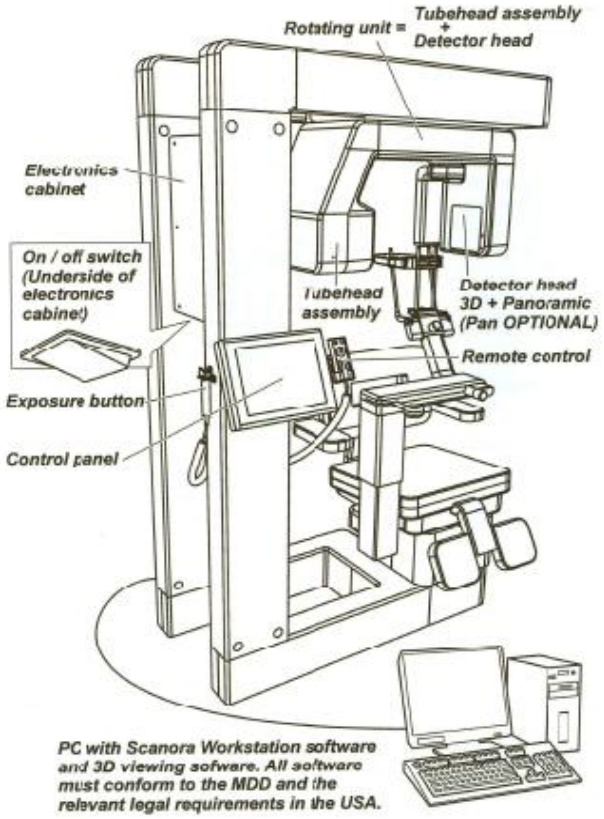

Figure 2.1: Major components of SCANORA 3D CBCT imaging system, with permission from Soredex, Tuusula, Finland [8]

2.2.1 Temporal bone Imaging

The standard imaging modalities for effective characterization of the complex anatomy of the temporal bone are multi-detector (or multi-slice) computed tomography and magnetic resonance imaging (MRI). However, the use of CBCT technology for temporal bone imaging is becoming popular in recent times. This is because it provides adequate visualization of the temporal bone and offers automatic 3D reconstruction of these images at a lower dose [15; 5; 57; 54]. As stated by Faccioli et al. (2009) [14], the effective dose of CBCT (Maxiscanner QR-DVT 9000, Verona, Italy) when compared with MSCT (Phillips, Eindhoven, Netherlands) is almost three times lower in temporal bone imaging. Despite the considerable dose saving permitted by CBCT, there is a need to improve its image quality, especially in temporal bone imaging [25; 27; 37; 51; 54].

2.3 Essential technical basis of CBCT

The major production process in CBCT imaging includes the acquisition of a series of 2D radiographs, reconstruction of the x-ray volume, and volume display and storage [21; 34; 51]. The CT process includes image acquisition that comprises an X-ray source, an object, a detector, and pre-processing that is often combined with image reconstruction in CBCT. It involves the calibration and the processing of the raw data acquired to yield projections. It comprises line integrals of the x-ray linear attenuation coefficient distribution associated with the object and image display and archiving.

2.3.1 X-ray generation and emission spectra

X-rays are generated in X-ray tubes when accelerated negatively charged electrons bombard targeted positively charged nuclei of high atomic number material such as tungsten [12; 13; 34; 56]. The electric field of the accelerated electron interacts with the target anode nucleus to release energy in the form of electromagnetic radiation (X-rays) called ***Bremsstrahlung*** or braking radiation. The Bremsstrahlung process X-rays have a continuous broad line energy spectrum (as shown in figure 2.2) and the X-rays generated are mostly with low energies. The energy of Bremsstrahlung photons ranges from zero to the maximum kinetic energy of the incident photons. ***Characteristics X-rays*** are the other type of X-rays produced alongside Bremsstrahlung X-rays. They are most useful in diagnostic radiology and are produced as excited electrons interact with the orbital electron [2; 12; 48; 52]. This results in transition of electrons between various orbital shells of the target atoms. They appear at discrete lines (as shown in figure 2.2) at a fixed energy in the X-ray spectrum and differ from the continuous energy spectrum of the Bremsstrahlung process [13; 48]. The fixed energy levels represent the differences between the binding energies of the electron orbital shells of the target atoms and are emitted when electrons make a transition from one atomic level to a lower atomic level. The process involves ionization of a high-energy inner shell (K-shell) electron that is then replaced by on outer shell electron that transits from the L, M, N, O or P shell. The shell where the transiting electron is travelling from determines the energy of the X-ray photons produced [12; 22; 34; 48; 56].

An X-ray spectrum is a graphical illustration of the relative number of X-rays produced at different X-ray energies (as shown in figure 2.2). It comprises the characteristic and the Bremsstrahlung X-ray photons [56; 34; 13]. The X-ray spectrum is of high importance in radiology because it influences the radiation dose and image quality. This is because X-ray distribution influences X-ray attenuation as the photons traverse objects of different densities and this effects image contrast. The voltage (kVp) determines the maximum X-ray energy (keV) of the spectrum and also influences the the number of X-rays produced. Additionally, X-ray tube potential and minimum filtration determines the average energy of the X-ray photons [4; 13; 22; 48].

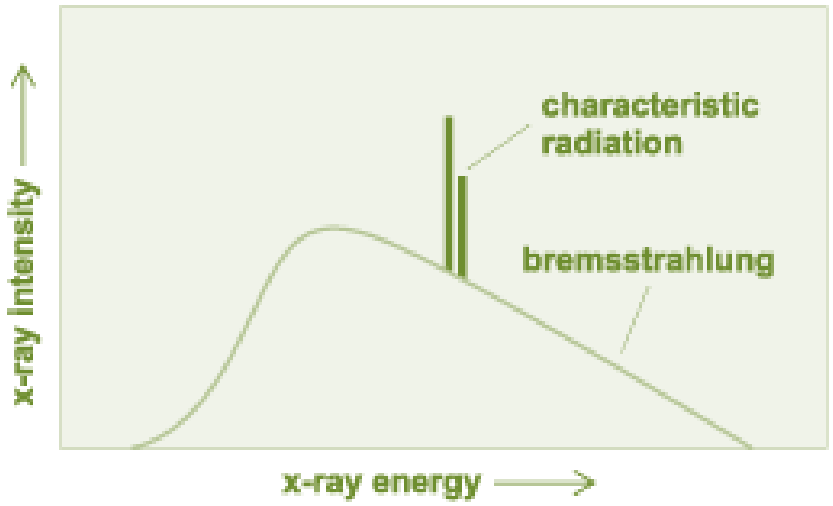

Figure 1.2: X-ray spectrum for an X-ray tube [13]

2.3.2 Attenuation and exposure parameter

The fate of X-rays that traverse through tissue includes: no interaction, complete interaction or partial absorption with scatter. The interaction of an X-ray depends on tissue density, tissue thickness, and X-ray energy (kVp). Highly dense anatomical structures such as bone attenuate more X-rays from the penetrating beam than less dense structures such as fat or muscle [19; 22; 48]. Three main physical processes that are responsible for the attenuation of an X-ray signal are photoelectric absorption, Compton scattering, and pair production. In the photoelectric effect or absorption, the total energy of an incoming X-ray photon is transferred to an inner electron that is then ejected. Compton scattering occurs when the incident photon interacts with an outer electron knocking out the electron. The incident electron loses a part of its energy and it

is deflected in a different direction. In pair production, the photon interacts with a nucleus forming a positron-electron pair. Any excess photon energy possessed by this pair is then transferred into kinetic energy in the particles produced [1; 12; 22; 48].

As the X-rays pass through the object being scanned, the signal is attenuated by scattering and absorption. The probability that a photon will penetrate through a patient or be attenuated is dependent on the sum of the X-ray attenuation properties of all the tissues the photon traverses to give the image of the patient [12; 13; 34; 43; 56; 43]. This probability may be expressed per thickness of the attenuator as the detected x-ray intensity by Lambert-Beer equation as:

$$I = I_0 \exp[\mu x] \qquad (2.1)$$

where I_0 is the initial X-ray intensity, variable *x* is the length of the object traversed by the X-ray photon and μ denotes the linear attenuation coefficient o0f the material being scanned [12; 13]. Taking into account the relationship between X-ray attenuation coefficient and the X-ray energy, solving the equation over the range of effective X-ray energy spectrum resolves equation 2.1 into equation 2.2:

$$I = \int I_0(E) \exp[\textstyle\sum_i(-\mu(E)x_i)]\, dE \qquad (2.2)$$

where E is the X-ray photon energy.

Higher kVp X-rays are less likely to interact with tissue and are described as more "penetrating". Increasing kVp, thereby generating more penetrating radiation, reduces the relative image contrast (or visible difference) between dense and less dense tissue.
In order to obtain optimum contrast in an X-ray image, one must adjust the photon energy spectrum for the X-ray photons to efficiently penetrate such an object [25]. This is done by adjusting the exposure parameters such as kVp, mAs and intensity (I). The peak kilovoltage (kVp), which influences the quantity of photons and their energy, is related to the intensity, I, so that:

$$\frac{I_1}{I_2} = \left(\frac{kVp_1}{kVp_2}\right)^2 \qquad (2.3)$$

As expressed above (see equation 2.3), the intensity of the radiation is proportional to the square of kVp change. Hence, a 50% decrease in mAs is equivalent to a 15% increase in kVp. Therefore, kVp changes have a major effect on the photon absorption

and patient dose. Despite the fact that mAs controls the number of electrons needed for X-ray formation, reducing the number of X-ray photons (mAs) has less of an effect when compared with the effect of kVp that quantifies the number of photons and their energy [1; 12; 25; 39; 55]. In summary, three reasons are clearly stated why increasing the average energy of photons (kVp) results in reduction in patient dose:

- some photons in the scattered low energy radiation receives sufficient energy to penetrate deeper than the skin surface, and thereby increasing image quality
- the number of photons engaged in the photoelectric effect will reduce as the average photon energy increases and the photons penetrates the object and contributes to image quality instead of increasing the radiation dose.
- more high-energy X-rays are made available for effective radiographic image density and contrast management even when the mAs is reduced [12; 13; 19; 34; 48].

2.3.3 Beam Filtration

Filters in CT devices are absorbers or attenuators placed between the X-ray source and the object. The beam attenuator filters out or absorbs the low energy X-rays that do not contribute to the image information, but increases the skin entrance exposure dose [11; 25; 51]. Inherent filtration and additional filtration are the two most common filtration types in CT devices. Inherent filtration reduces the skin dose and is provided by the X-ray tube glass, lead tube housing, cooling oil and window [1; 11; 22; 25]. The additional filtration is a removable filter(s) that further reduce the entrance skin exposure (ESE) to the patient without altering the image quality [34; 51; 55]. The additional filtration compensates for variations in beam path length across the patient cross section and may be in the form of several millimetres thick aluminium or its equivalent. According to regulations and manufacturing standards for X-ray equipment, the radiation from an anode of an X-ray tube must pass through some type of filtration or through a beam attenuator [48; 56].

The spectrum of X-rays emitted by CT devices induces a wide range of energies that can be reduced using filtration (Figure 2.3.) After filtration, the X-ray beam is said to be

"hardened" meaning its average energy has increased giving the beam a higher quality in terms of uniformity, contrast, and linearity [22; 48; 56].

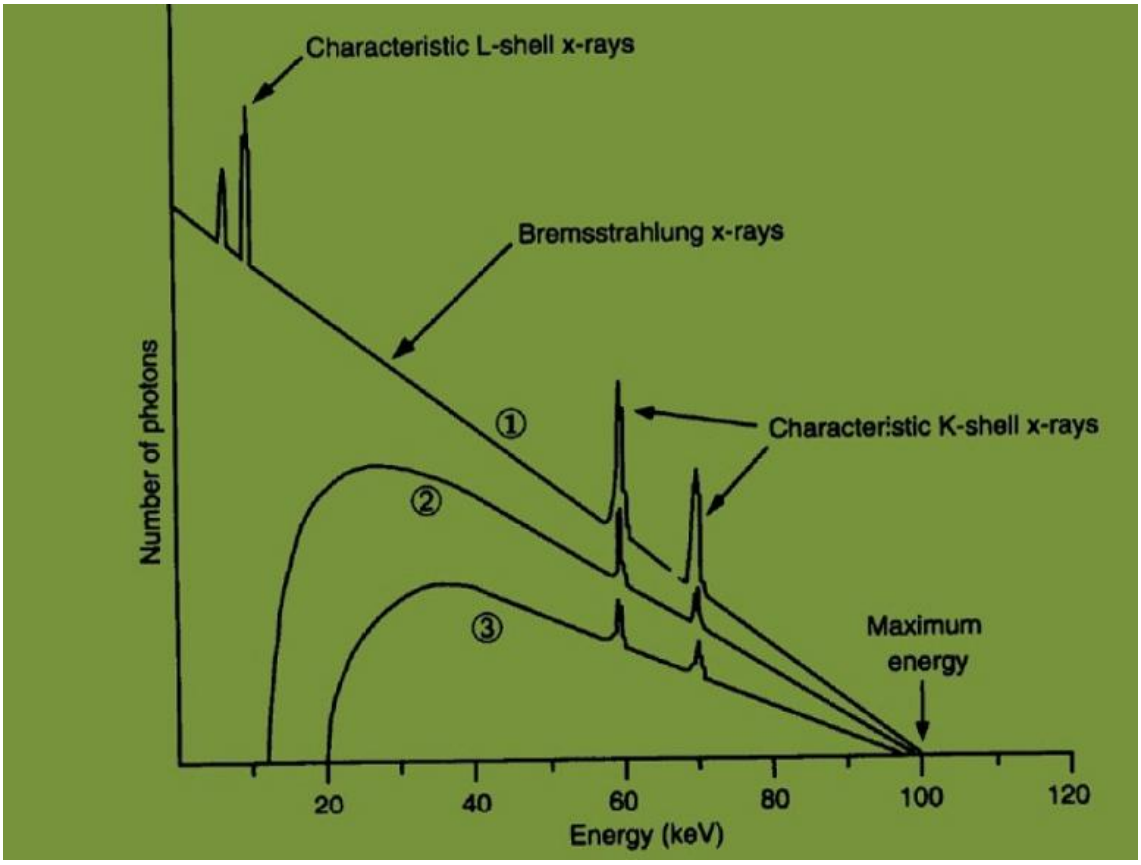

Figure 2.2: The energy spectrum showing the effect of filtration (1) spectrum exiting the anode, (2) After inherent filtration, (3) After additional filtration [22].

The half value layer (HVL) is a commonly used method for describing the penetrating ability and filtration of specific radiations. The HVL (measured in cm or mm) is the thickness of a given material that is required to reduce the initial beam intensity of a radiation by one half [11; 25; 27; 34; 59]. Additionally, a relationship exists between the HVL and the attenuation coefficient. This relationship is represented in the following equation 2.4 [22; 59]:

$$\text{HVL} = 0.693 \text{ X Average Range} = \frac{0.693}{\mu} \qquad (2.4).$$

where μ denotes the linear attenuation coefficient of the material being scanned.

However, the thickness and type of filter material are two important parameters in filtration. Furthermore, the type of filter, in relation to the atomic number of the material used, is also another important factor in filtration. As the atomic number (Z) of copper

(29) is higher than aluminium (13), aluminium is sufficient for lower energy X-rays whereas for higher energy X-rays, copper or tin with aluminium may be used [19; 25; 29; 34; 41; 52; 59]. This is because materials with a high atomic number have a higher attenuation coefficient. Thereby, only X-rays with high enough energy are allowed to penetrate these materials [13; 22; 25]. An example of this happens in the compound type filtration set-up [25] where the material with the highest atomic number is placed first in the path of the X-ray beam followed by the material with a higher atomic or low atomic number, depending on the number of filter materials inter-positioned [25]. In addition to aluminum, which has been used in conventional CT as standard, other materials such as copper (Cu) and tin (Sn) are used as filters in CT imaging [25; 29; 34; 59].

The SCANORA 3D CBCT device (Soredex, Finland) used in this study was fitted with two filters one in the tube and one in the collimator (Fig 2.4).

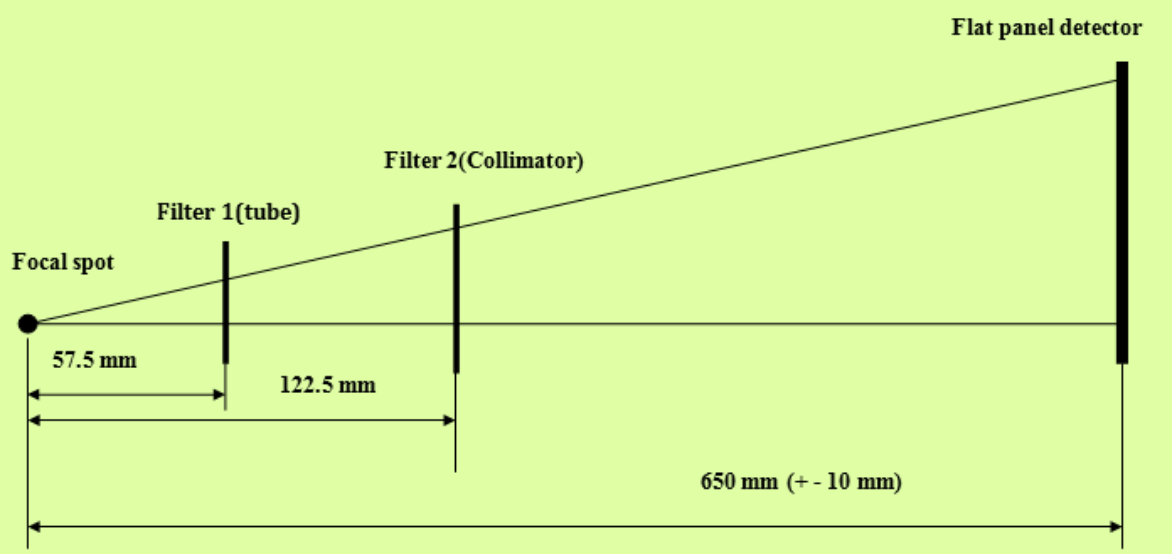

Figure 2.4: Illustration of the distance between the Focal point and flat panel detector showing the position of filter 1 (tube) and filter 2 (collimator).

The collimator restricts the X-rays from scattering and helps maintain a chosen region of interest. Combining the two filters enhances beam hardening, beam uniformity, and the focusing of the X-rays, and, thereby, increases image quality [19].

2.3.4 Field of View (FOV)

The field of view (FOV) determines the depth within the patient that can be imaged or visualized. This feature is perhaps one of the most important in controlling patient radiation dose. The FOV in CBCT is one of its unique features [12; 37; 51] as it limits the field size to the region of interest (ROI). This offers a huge benefit to the patient as only the area to be diagnosed is irradiated by the X-ray beam. This reduces the patient dose and also benefits the radiography as the amount of scattering is lower when the ROI is locally irradiated. Furthermore, its efficiency depends on the manufacturer's detector size, shape and beam geometry and can be selected to suite different types of examinations. However, scanners using image intensifiers and CCD detectors use cm^3 in describing their dimensions. The dimensions of the beam's cylindrical FOV can vary from small fields for dental imaging to large fields for other facial examinations [37; 51; 55]. In addition, the mode options may include facial (scout or 3D), panoramic, implant, and dental options chosen according to the examination [8]. The pixel size and matrix size, which are important in deducing image quality, are related to FOV according to the following equation [49]:

$$\text{pixel size} = \frac{Field\ of\ view}{matrix\ size} \tag{2.5}$$

Offset mode/ Extended FOV scanning: Some CBCT devices (SCANORA 3D) offer an offset scanning mode. The offset scanning mode is used to increase the width of the FOV and, thereby, only use a small area of the detector. This is done by collimating the beam asymmetrically and offsetting the position of the detector in such a way that it scans only half of the patient (including the region of interest). This method is said to allow the scanning of an image larger than the flat-panel detector [51]. The acquisition of images larger than the flat-panel detector (extended FOV) is possible with the use of offset mode scanning as displayed in Figure 2.5:

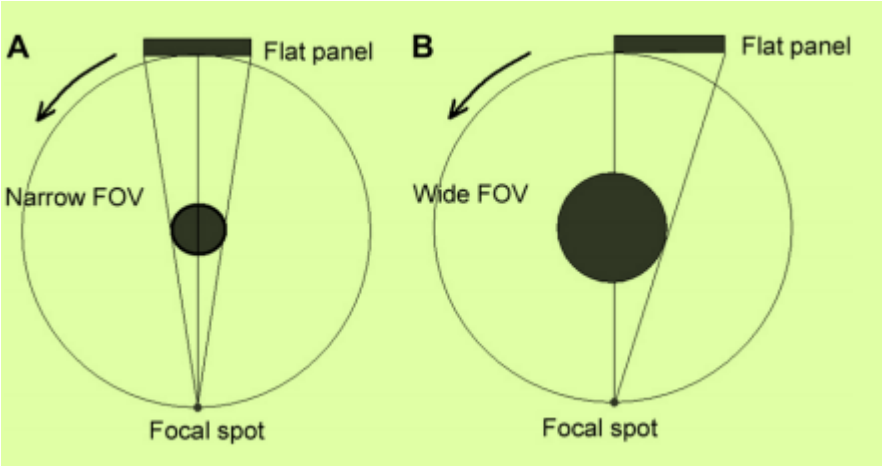

Figure 2.5: (A) is an image of the normally used geometry of acquiring images from the focal spot of the X-ray tube to the flat panel detector (B) is an image of the extended FOV, it collimates the beam asymmetrically to extend the FOV object and shifts the location of the detector. (Courtesy: Soredex, Helsinki, Finland: with permission) [51].

2.3.5 Number of projections

The number of projection images that make up the data set may vary depending on the type of device used. This number is determined by frame rates (number of images recorded per second), and the exposure cycle and the rotation speed [21; 30]. Increasing the projection data by increasing the projection increases the amount of information available to reconstruct the image. Following the ‘‘as low as reasonably achievable’’ (ALARA) principle to produce images of diagnostic quality, the number of frame images should be minimized as acquisition of a large number of frame images requires a larger amount of radiation dose, longer scanning times, and longer primary reconstruction time [21; 51].

Temporal bone imaging is mostly carried out using 150% number of projections [50; 59]. This is because enhanced and high quality images are required to effectively characterize the flexible anatomical structures in this region. Even though the 150% number of projections is known to increase the radiation dose by a certain percentage, it is acceptable for this purpose as the radiation dose used in CBCT is quite low [50].

2.3.6 Radiation dose

In order to balance the difference between quality and radiation dose in CBCT, the choice of settings (kVp and mAs) used during the exposure is of major importance. The use of collimation and low mAs aids the reduction of the effective dose but leads to the formation of low quality images [28; 34]. Despite the ease of obtaining diagnostic images through digital radiographic imaging, one must justify the need for every diagnostic protocol done on a patient before carrying out the radiation exposure [42; 63]. This is because the radiation dose delivered during a CT scan is always more than that administered for an equivalent radiographic image. The international Commission on Radiological Protection (ICRP), an independent international body formed to deliberate on policies in the field of radiological protection, define strict regulations on the use of radiation in medical imaging. Their policies are based on the linear no-threshold (LNT) theory of radiation carcinogenesis (ICRP 2008). These policies are for the prevention of cancer and other diseases and the effects associated with exposure to ionizing radiation, and to protect the environment. The regulations focus on the following:

- The current understanding of the science of radiation exposures and effects.
- The value judgment taking into account societal expectations, ethics, and experience gained in the application of the system [28; 42; 63].

Several quantities and ambiguous terms are used to measure the amount of ionizing radiation a patient is exposed to depending on the application [61]. These metrics are explained in the following headlines:

CT dose index 100 (CTDI 100): It creates an index that shows the average dose to a phantom in the centre of the scan and it is presently the guidance offered by the Food and Drug Administration (FDA) for CT equipment manufacturers with provision of the U.S. federal performance standard for CT systems. It is mathematically given as follows:

$$\mathrm{CTDI}_{100} = (1/nT)\int_{-50mm}^{+50mm} \mathrm{D}(z) \qquad (2.6)$$

The term D(z) is the dose profile along in the air at position z of the dosimetry phantom, z is the position along a line perpendicular to the tomographic plane, n is the number of

tomograms produced in a single scan and T is the nominal tomography section thickness [61].

The effective dose: This is used as a measure of the radiation dose absorbed by patients in a radiographic modality. Effective dose measurement and calculation in practice is carried out using an anthropomorphic phantom, representing the shape and attenuation of an average human, most commonly an adult male. The effective dose ranges from one examination to other and also has different values in different organs. However, effective dose is influenced by technical imaging parameters such as mAs and FOV. For large FOV in CBCT scanners, the effective doses are higher and also depend on tissue type and the scanner's properties [42; 63]. Mathematically, effective dose measured in sievert (Sv) and is calculated thus:

$$E_T = W_T H_T \quad (2.7)$$

where H_T is the equivalent dose or radiation weighted dose for all organs or tissues T measured in sievert (symbol: Sv) and W_T is the tissue weighting factor that expresses the contribution of this tissue to the overall radiation detriment from

$$H_T = W_R \sum fD_T \quad (2.8)$$

The variable W_R denotes the radiation-weighting factor (being 1 for X-rays), and f is the fraction of tissue T. D_T denotes the average absorbed dose of tissue T (measured in unit Gray, Gy) and the summation being over all slices [42].

The major feature of CBCT imaging lies in the intensity of its ionizing radiation. It is known for its lower radiation dose compared with conventional CT used for ear exploration and other applications. Depending on the manufacturer, model, selected FOV, other imaging parameter selection and the material to be imaged, the radiation dose varies for all types of exposures. However, the study of Faccioli et al. (2009) confirmed that the effective dose of CBCT when compared with MDCT in temporal bone imaging is lower [14]. In addition, the amount of improvement in signal-to-noise ratio (contrast resolution), spatial resolution and slice thickness will determine the number of times the patient dose has been increased [14; 19; 37]. In addition, reducing tube current (mA), appropriate beam collimation to restrict the X-ray beam to the ROI, exposure time length, and choice of kVp are technical factors that have an effect on radiation dose [36]. The relationship between resolution and dose can be deduced as:

$$D = a\left(\frac{S^2}{b.e^3}\right) \quad (2.9)$$

The variable D is the patient dose (measured in rad), S is the signal/noise ratio, e is the spatial resolution, b is the slice thickness, and variable a is a constant.

2.3.7 Image Detection

High resolution flat panel detectors (FPD) used in CBCT devices allow the generation of projection images of an entire region of interest (ROI) from a single gantry rotation by capturing the diverging cone-beam shaped x-rays [1; 12]. The size of this detector determines the extent of the object that is averaged into a single reading and its configuration is based on a solid-state large area integrated circuit. The detector comprises a large pixel array of thin film transistor made of amorphous silicon photodiodes and a cesium iodide (CsI) scintillator [51]. In an FPD, the scintillation material (CsI) indirectly detects and absorbs the incoming photons (X-rays) that have passed through the patient. These photons produce flashes of light in proportion to the intensity of the absorbed X-rays. Photodiodes record the flashes of light produced by the scintillation crystals and transform them into an electric charge in proportion to the light absorbed. The electric charge in turn is converted into electronic data that a computer can convert into a high quality image of the target [12; 19; 27; 34; 51].

Flat panel detectors (FPD) rotate very quickly at a range of 10-30 seconds and require frame rate image acquisition times of a few milliseconds [12; 51; 55]. The major advantages of FPD are fast digital read-out, reduced peripheral distortion, less noise, greater sensitivity to X-rays, and high spatial resolution. It also provides a greater dynamic range compared with conventional detectors such as an image intensifier detector [12; 37; 51]. Despite the advantages offered by flat panel detectors, one major disadvantage is the bad pixels' formation that limits the performance of the detectors in relation to the linearity of response to the radiation spectrum [37; 51]. Bad pixels formation also causes less uniformity of the incident photons throughout the detector and its effect on image quality is most noticeable at lower and higher exposures [37; 51]. It is essential that the FOV used during an exposure is smaller than the detector size. According to the principle of CT, the imaging region of the scanned object must fit

within the X-ray beam formed by the X-ray generator and the detector. Usually, it is difficult to image an object that is larger than the scan FOV as the image does not effectively represent the object [1; 12; 37; 59].

2.3.8 Image Reconstruction

Image reconstruction is done immediately after the acquisition of the projection images. It involves processing projection frames or tomographic slices to create volumetric data by dividing the volume into its constituent elements called voxels [1; 21; 37; 51]. Figure 2.6 presents this reconstruction method. This is done mathematically by converting sinograms (a composite image that relates each row of projection images) into two-dimensional slice images and the raw intensity data present in the sinogram are also converted into CT numbers (Hounsfield unit). These CT numbers then correspond to the gray scale in the image. The steps used in the reconstruction process are as follows: sinogram formation and correction by Radon transformation, and processing the corrected sinogram using an algorithm [1; 11; 21; 27; 37; 51; 55]. Radon transformation is done by extracting rows that later form a composite image [19; 27; 37; 51].

The Feldkamp, Davis, and Kress (FDK) filtered back-projection algorithm is often used for processing the CBCT sinogram [19; 34; 51; 65]. In this filtered back-projection technique, the projection data is weighed and then convolved with a filter. Then, each view is successively superimposed over a square grid (back-projection) at an angle that corresponds to its acquisition angle [19; 27; 34; 51].

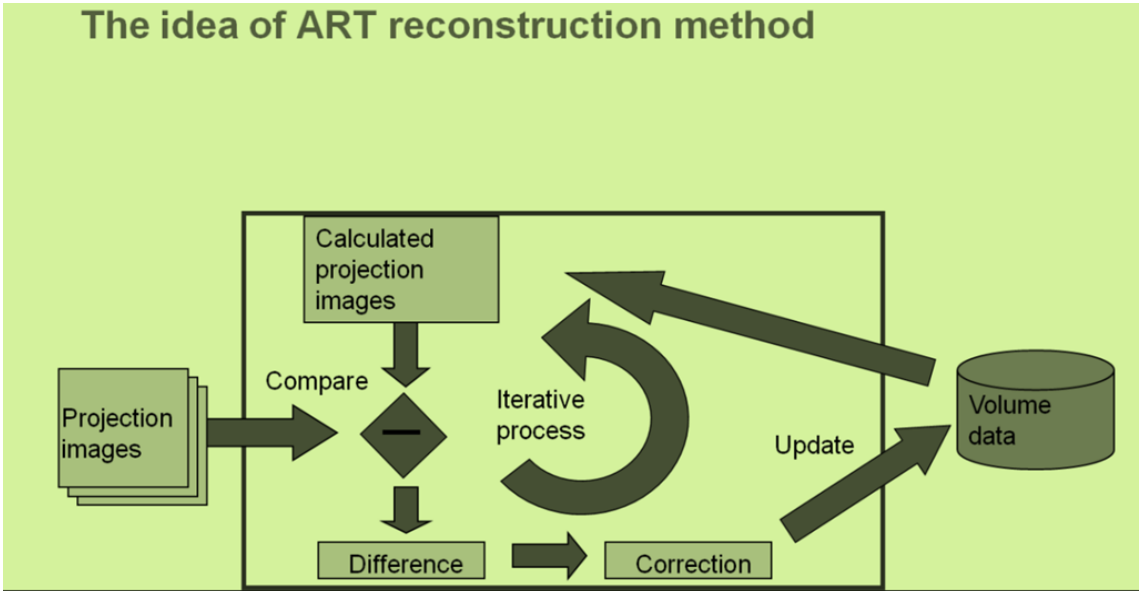

Figure 2.6: The steps involved in ART reconstruction used in SCANORA 3D Cone-Beam 3D Imaging System for projection data reconstructions (courtesy of Soredex, Helsinki, Finland: with permission).

In CBCT reconstruction, primary reconstruction images are used to create secondary 2D reconstruction images in three orthogonal planes (axial, sagittal and coronal) and the production of 3D views. Primary reconstruction contains individual projection frames ranging from 100 to 600 images with each image having over one million pixels, with 12 to 16 bits of data assigned to each pixel. Due to the complexity, data handling is done by an acquisition computer that stores raw projection images and a workstation platform that receives the data from the acquisition computer via Ethernet and serves the purpose of processing the raw projection data [37; 51]. Sub-millimeter isotropic voxels with compositional equality in its three dimension (x=y=z) with a resolution that ranges from 0.076 mm to 0.4 mm [51] are produced in CBCT. This provides excellent high-contrast resolution and accurate spatial resolution even in the secondary (axial, coronal, and sagittal) and multiplanar reformation (MPR) images (formed by the stalking of the image). Additionally, isotopic pixels are preferable where high precision in all dimensions are of necessity. An example of this is when an implant site assessment, such as a cochlea implant that is of high interest in temporal imaging, is of necessity [27; 37; 55].

The total time for reconstruction depends on the acquisition parameters (number of projections, voxel size, and FOV) as well as the hardware (speed of processing and

transfer of data from acquisition computer to workstation) and the software (reconstruction algorithm) used. The time for reconstruction must be within a range of 2-3 minutes for standard resolution scans for efficient patient flow [51]. Hence, filtered back-projection is said to be fast and deterministic with a very well understood principle grounded in Radon transform and the Fourier slice theorem that links a function and its projections to its Fourier transform [12; 27; 37].

2.4 Image Quality Analysis

One of the most important functions of a CT system is to resolve a 3D structure and represent that structure as an accurate 2D cross-section on a screen. There are several characteristics that affect the effectiveness of a CT system in delivering efficient image quality when carrying out this task [2; 49; 52]. Spatial resolution, contrast resolution, linearity and noise are the primary characteristics that determine the clarity of the information a medical image conveys [19; 49; 52]. The clarity of an image is acceptable if it is clear and unambiguous. However, CT parameters such as material thickness, algorithms, field of view, and detector size also affect the overall image quality in CT. These parameters must be balanced alongside with the characteristics in order to produce the best possible image of the anatomical structures being scanned [17; 19; 37]. Among other parameters necessary for effective image quality, the ability of the observer to detect signs of pathologically important processes is a major factor that should be noted during image acquisition [2, 17; 27; 55]. On the other hand, noise and artifacts have adverse effect on image quality as they distort or hinder image quality. It is necessary to manipulate CT parameters effectively in order to eliminate or reduce the effect of noise and artifacts.

2.4.1 Spatial Resolution

Spatial resolution is the ability to resolve, as separate forms, the smaller of two objects that are located very close to each other [49; 52]. Pixel size, focal spot size, source-object-detector distance, detector width, blurring, ray sampling and patient motion are factors that may affect spatial resolution in CBCT [2; 12; 49].

Several methods that quantify or measure spatial resolution in CT systems include point spread function (SPF), line spread function (LSF), edge spread function (ESF) and modulation transfer function (MTF) [2; 27; 36; 49; 52; 63].The MTF is the most commonly used method to measure the spatial resolution capabilities of a CT system. It is the ratio of the amplitude of spatial frequency at the output from the imaging system to the amplitude of the same spatial frequency at the input to the imaging system [63]. In order to determine the MTF's for CT scanners, a measurement must be performed to obtain either the LSF or the PSF. Thereafter, the usual procedure is to interpolate between the measured points and to determine the Fourier transforms numerically in order to obtain the MTF [19; 49; 52; 63]. Apparently, the value of MTF varies from unity to zero. At low spatial frequencies, MTF is unity for all spatial resolution and it decreases as the spatial frequency increases. When the value of MTF becomes zero, it means that no information is available to be seen [63]. MTF is mostly represented graphically and it describes the blur or resolution property of any imaging system [2; 52; 55; 63].

2.4.2 Low-contrast Resolution

Low contrast resolution or the sensitivity is the ability of an imaging system to discriminate between two anatomical structures that attenuate nearly the same amount of X-ray photons. The small attenuation differences in such images are due to the slight differences in densities or atomic number of the objects [36; 49]. Additionally, the absorption property of any tissue is often represented by the linear attenuation coefficient of such an object. This is a number that describes the absorption characteristics of the tissue and it is dependent on the photon energy, material thickness, density, and atomic number [25; 29; 34; 41;].

2.5 Artifacts

Artifacts are related to unwanted distortions or errors that impair image quality and influence the correct assessment of details of interest, and thus, render the images diagnostically unusable [1; 30; 51]. In order to enhance an image affected by artifacts, there is the need to understand the basis of these artifacts and how they can be tackled [1; 30]. These artifacts are categorized according to their origin as physics-based,

patient-based, and scanner-based artifacts. Physics-based artifacts are caused by the physical processes (i.e. the polychromatic nature of the x-ray beam). Patient-based artifacts result from patient movement or the presence of metallic substance in the object to be scanned. The scanner-based artifacts are mostly caused by the imperfections in scanner functions such as calibration errors and scanner detection issues and are mostly presented as ring artifacts [1; 30; 51; 63].

2.5.1 Image Noise

Noise in its simple definition is the measure of the standard deviation of voxel values in a homogenous phantom [36]. Image noise originates as unwanted random or non-random distributed fluctuations of the signal that interferes with the image quality by obscuring the information content of an image [30; 63]. It is a form of physics-based artifact that reduces the low contrast resolution of an image. Thereby, it makes it difficult to differentiate between two tissues with similar densities [17; 36; 63]. This poses a challenge as the images acquired can be difficult to segment or use for treatment planning and follow-up in CBCT. To analyze the noise content of an image, the standard deviation of CT numbers in a region of interest must be calculated [19; 30]. The magnitude of noise present in a medical image is influenced by increment or decrement of one or more combinations of the following: kVp, mA, exposure time, object size and shape, collimation/reconstructed slice thickness, reconstruction algorithm or filter, detector efficiency, focal spot to isocentre distance, and the size of the focal spot [11; 25; 30; 36; 52; 63]. Noise in CBCT originates from quantum mottle or the fluctuation of photon fluency in the x-ray quanta. The number of detected quanta varies across different measurements probably due to statistical fluctuations that arise in the counting process [17; 63].

In physics, the scatter-induced noise arises from the interactions of the incident X-rays with the atoms in the imaged object. During the traversing of the X-rays through the object, photoelectric absorption, Compton scattering, and coherent scattering may occur [30]. In radiology, most of the interactions can be traced to Compton scattering that results from the interaction between the incident high-energy X-ray photon and one of the loosely bound outer shell electrons on the atom of the object to be imaged. This leads to the ejection of this loosely bound electron whose energy and direction depends

on the energy transferred to it as it is ejected [12; 30]. Noise degrades the image quality produced with CBCT imaging devices more when compared with conventional CT devices due to the lower mAs values [30].

Standard deviation: The standard deviation, evaluated from mean is a simple and useful tool in characterizing the noise in a medical image. It shows how far the values on a window deviated from their average. To evaluate the standard deviation in two or more identical images, one must measure the x_i (specific area with equal number of pixels) in each image and evaluate the standard deviation of this region [4; 6]. In most medical images, it is difficult to evaluate the standard deviation because of motion artifacts. If we assume that the signal or image is the same with only statistical fluctuations, such as in this study, in every location in the region of interest, then the noise (standard deviation) can be calculated from one image and the same can be done for more images obtained from the fixed anatomy from a similar region. Mathematically, standard deviation can be calculated using the following equation [4; 6; 46]:

$$\sigma = \left(\frac{1}{n}\sum_{i=1}^{n}(x_i - u)^2\right)^{½} \quad i = 1,2,3 \dots \dots 30 \qquad (2.7)$$

where u is the mean of pixel values in the ith image window. In this thesis, σ would be estimated in a 30-by-30 matrix extracted from similar points in all the images.

2.5.2 Beam Hardening

The most commonly encountered artifact in CBCT scanning is beam hardening. This causes the edge of an object to appear brighter than the centre even when the material is homogenous. This occurs when imaging bony regions whose densities may vary depending on the type of bone and location of the anatomy. In beam hardening, there is an increase in mean X-ray energy or "hardening" of the polychromatic X-ray beam, which is composed of photons of various energies in its spectrum, as the beam traverses the object [1; 27]. Although the beam loses energy overall, its average energy increases, and, thus, affects the effective attenuation coefficient. This conflicting information confuses the reconstruction algorithm and the object appears less dense than it actually is. This manifests as two different artifacts within the reconstructed image, namely:

cupping artifact, and streaks and dark bands [1; 12; 30; 63]. These artifacts are explained below.

Cupping artifacts: This refers to the differential absorption between the X-rays passing through the centre of an object where there is more material and those passing through the edges resulting in the formation of a "cup". The cup occurs when there is an artificial darkening in the interior of an image and a corresponding brightening near the edges of the image. The attenuation is said to reduce as the beam becomes harder leading to the creation of a new resultant linear attenuation coefficient profile that is different from the ideal profile obtainable without beam hardening [1; 12; 27; 30; 51; 55].

Streaks and dark bands are the appearance of dark bands or streaks between two or more dense objects that form a heterogeneous cross-section and result in artifacts. Streaks and dark bands are due to the difference in the portion of the X-ray beam that penetrates one object at a certain tube position when compared with the portion of the beam that penetrates the heterogeneous cross-section at other tube positions. The beam is said to be less hardened as it penetrates the heterogeneous cross-section and makes it difficult to differentiate between beam hardening artifacts and actual material variations. This is because the surfaces present in these tissues have different densities and attenuation profiles [1; 17; 30; 55; 63]. Severe streak artifacts may also occur due to photon starvation that causes noisy projections at tube angulations. This can be corrected by increasing tube current [1].

Beam hardening is unavoidable in CBCT scanning and it is a major concern of the manufacturers of these systems. Certain built-in features are available and many manufacturers are interested in research on new methods to minimize beam hardening [1; 30; 55]. The simplest approach to reduce this artifact is to use an energetic and uniform X-ray beam. However, an additional filter called a bowtie filter may be used to further harden the edges of the beam that penetrates the thinner part of a patient. Beam hardening correction software is used in iterative algorithms during image reconstruction of bony anatomy. It minimizes the blurring effect at the bone-soft tissue

interface and may also eradicate dark band appearances in non-homogeneous cross-sections [1; 30; 40; 51; 55]

2.5.3 Partial Volume Artifact

Partial volume artifact occurs when the X-ray scanner losses information while trying to average out the difference between a small number of high-density tissues and a large number of low-density tissues [1; 30; 40]. It appears as inherent resolution limitations and causes blurriness at the material boundaries of the image. The partial volume effect may also result from the penetration of other than the ROI of the cone-shaped beam that leads to the formation of pixels that do not represent the tissue or its boundary [27; 30]. Moreover, partial volume, which poses a problem in CBCT, does not affect image quality in MDCT devices. This is because the problem of insufficiency in detector size does not occur in MDCT while imaging objects. In CBCT, the flat-panel detector may be small for imaging certain objects. For this reason, the data reconstruction algorithm assumes that the object is entirely covered by the detector at all angles, whereas, some portions are missing. Then the reconstruction algorithm tends to calculate the linear attenuation coefficient of such an image based on the area covered. This result in inappropriate data collection as less data than what is represented by the object is in the FOV coverage. This often leads to truncated-view artifact [51].

In some cases, the artifact may result from a dense object located off-centre. It is caused by the presence of an off-centre object that lies on the pathway where the beam passes. As a result, the beam penetrates this off-centre object and registers its image on the detector coupled with the targeted object's image [1; 30]. Smaller FOV machines experience this phenomenon more than systems with a larger FOV. However, scanning using thinner slices instead of a few thick sections may minimize or avoid partial volume artifact and the voxels becomes smaller, and, hence, reduces the partial volume effect [1].

2.5.4 Undersampling

The number of projection images used in image reconstruction plays a major role in image quality. Undersampling occurs when there are too large intervals between projections or too few basis projections [1; 51]. Undersampling results in the misregistration of details relating to sharp edges, noisier images, and small objects, and may cause view aliasing or ray aliasing. View aliasing occurs in an image when fine lines or stripes appear to be radiating from the edge of a dense structure at a distance where ray aliasing occurs when the stripes appears close to the structure [1; 51]. This aliasing is said to be less serious in medical imaging especially in bony anatomy evaluation since the fine lines do not resemble the anatomical structures. However, when resolution of fine details is of high value, there is a need to avoid this form of artifact. Acquiring a large amount of projection data by increasing the projection is one way to minimize undersampling.

3. MATERIALS AND METHODS

One formalin-fixed human cadaver head of a succumbed Finnish patient with intact anatomical structures was scanned using the SCANORA cone-beam 3D imaging system (Soredex, Finland). The donor cadaver was obtained with permission from the Ethical Committee and the Department of Anatomy, Tampere University Hospital, Tampere, and was previously embalmed and stored in the standard fashion for use in teaching and dissection. The brain had been removed from the cadaver and the cranial cavity was replaced with a water-filled plastic bag. The cadaver head was fixed to a head support as shown in Figure 3.1 and the temporal region of the cadaver head was targeted by X-rays. Laser light beam markers were used to ensure the correct positioning of the cadaver head (Fig 3.1).

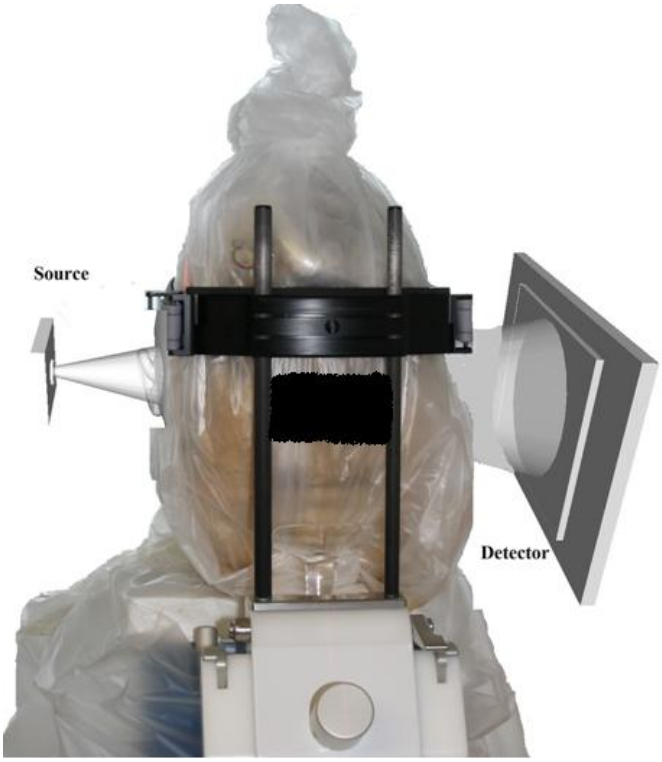

Figure 3.1: An Image of the cadaver head correctly fixed in the patient position to focus the beam on the temporal area of the cadaver head.

3.1 Image acquisition

Three different filter sets were used during image acquisition. In total, 10 scanning protocols were performed. The exposure parameters, number of projections (frames/scan) and filtration used in each scanning session are shown in Table 3.1. The acquired images were then transferred and reconstructed on a Phillips workstation using 0.51 mm slice thickness, 0.53 mm slice distance with no contrast enhancement or windowing.

Table 3.1: Imaging modes, exposure values, number of projections and filtration.

FOV (Z*XY)	Voxel Size (mm)	kV	mAs	frames/ scan	frame count	exposure time (s)	pulse length	imaging time	filter-1 tube	filter-2 collimator
60X60mm	0.133	90	12.5	450	450	4.95	11	19.95	0.1mm Cu	0.1mm Cu
60X60mm	0,133	90	8	450	450	4.95	11	19.95	0.1mm Cu	0.1mm Cu
60X60mm	0.133	90	12.5	675	675	7.43	11	29.93	0.1mm Cu	0.1mm Cu
60X60mm	0.133	90	8	675	675	7.43	11	29.93	0.1mm Cu	0.1mm Cu
60X60mm	0.133	90	12.5	675	675	7.43	11	29.93	0.1mm Cu	4 mm Al
60X60mm	0,133	90	8	675	675	7.43	11	29.93	0.1mm Cu	4 mm Al
60X60mm	0.133	90	12.5	675	675	7.43	11	29.93	3 mm Al	4 mm Al
60X60mm	0.133	90	8	675	675	7.43	11	29.93	3 mm Al	4 mm Al
60X60mm	0.133	90	12.5	450	450	4.95	11	19.95	3 mm Al	4 mm Al
60X60mm	0.133	90	8	450	450	4.95	11	19.95	3 mm Al	4 mm Al

3.1.1 Cu-Cu (factory-fitted) filtration study

The first filter set (factory-fitted filter set) consisting of one 0.1 mm Cu and one 0.1 mm Cu were positioned as shown in Figure 3.3. Four scanning protocols were carried out with this filtration (Table 3.1). Out of the four scanning protocols, two of the scanning protocols were carried out using 100% projections and the remaining two were done using 150% projections.

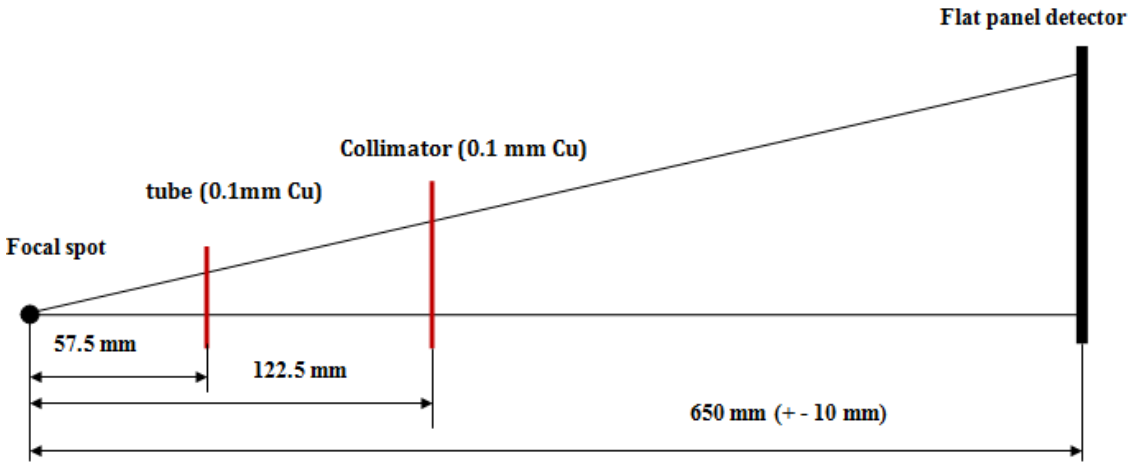

Figure 3.3: The distance between the filters and their distances from the source and the detector.

3.1.2 Cu-Al filtration study

In this study, the first Cu filter in the tube was retained and the second Cu filter in the collimator was removed and replaced with a 4 mm Al filter (figure 3.4.) Recalibration of the device followed and two scanning protocols (Table 3.1 row 5 and 6) were performed at 150% number of projections.

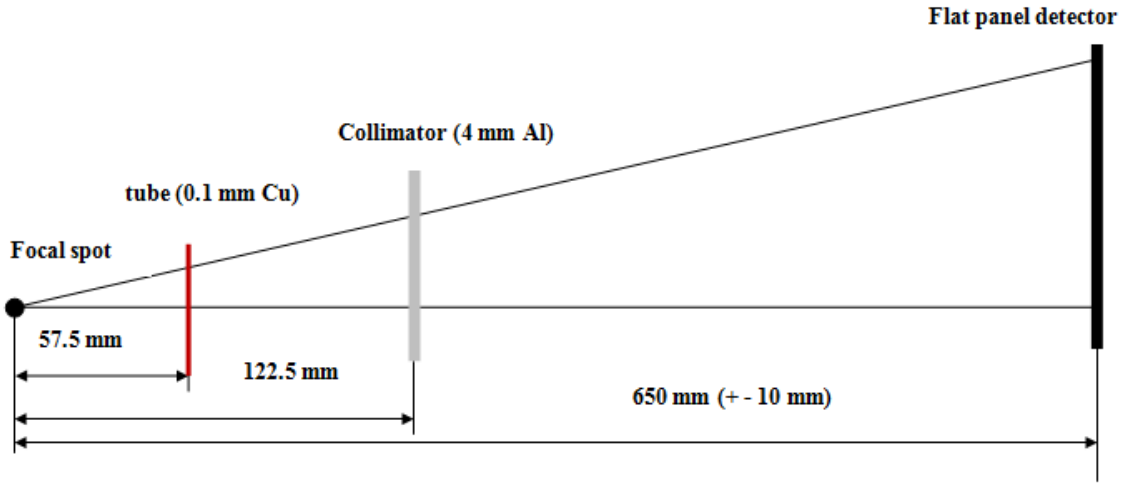

Figure 3.4: Arrangement of the filters showing the distance between the filters and their distances from the source and the detector.

3.1.3 Al-Al (custom-made) filtration study

In this study, custom-made Al-Al filters of a thickness of 3 mm and 4 mm were fitted in the tube and collimator filter positions respectively (shown in Figure 3.5). Recalibration of the system followed and four scanning protocols were carried out. The exposure parameters and filtration used in the four scanning protocols are displayed in Table 3.1. Two of the scans were carried out at 100% projections and the remaining two were carried out at 150% projections. The distance between the two filters remained the same as in the first study. As shown in Figure 3.4, the space between the filters (65 mm) and the distance between the filters and the detector (527.5 mm +- 10 mm) remained the same.

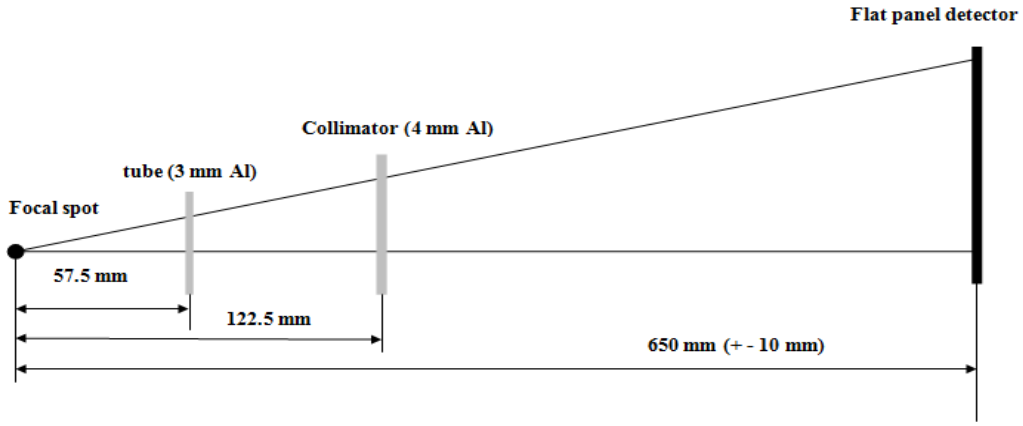

Figure 3.5: Arrangement of the filters used for study 2 showing the distance between the filters and their distances from the source and the detector

3.2 Quality assessment

All images were exported to a Phillips workstation to perform coronal, sagittal and axial reconstructions using 0.53 mm slice thickness and 0.51 mm slice distance. The two forms of assessments carried out are explained below.

3.2.1 Quality assessment based on visual assessment

All images were exported to a Phillips workstation to perform coronal, sagittal and axial reconstructions using 0.53 mm slice thickness. Visual image assessments were performed on 83 coronal, 90 axial, and 85 sagittal slices obtained from ten scanning protocols. The following nine anatomical landmarks were visually assessed by two radiologists with more than 20 years of experience: (1) the tympanic membrane, (2) the

incus, malleus and stapes, (3) the scutum, (4) the oval window, (5) the cochlea, (6) the vestibulum, (7) the semicircular canals, (8) the Eustacian tube, and (9) the facial nerve canal. The effect of changes in the type of filtration, mAs, and the number of projections on the image quality of each of these anatomical structures was scored according to the following ranking system: (0) absent, (1) hazey, (2) sharp, and (3) very sharp.

3.2.2 Quality assessment based on noise analysis

The second part of the quality assessment focused on calculating image noise. The noise in a chosen image was characterized by evaluating the standard deviation. Identical slices were selected from the coronal data sets of all the images used in the visual assessment. Then x_i (30-by-30 selected pixel) and u (mean value over the 30-by-30 pixels) were calculated. The standard deviation, σ, of the separate pixel values in the image was then calculated using the following equation [4; 6; 46]:

$$\sigma = \left(\frac{1}{n}\sum_{i=1}^{n}(x_i - u)^2\right)^{½} \quad i = 1,2,3,4,5, \ldots \ldots 30$$

In all the images evaluated, similar ROIs representing a 30-by-30 matrix were cropped (shown in Figure 3.5) using algorithms (Appendix 1) and the standard deviation was calculated for each image. The standard deviation was chosen as a mean of noise assessment in this study because the cadaver head used was fixed and the images acquired from the same position in each case were identical. The evaluation was carried out in MATLAB user interface and the generated results are presented in the results section [46]. Figure 3.5 shows one of the identical slices and the 30-by-30 pixel from the region of interest used for the standard deviation evaluation.

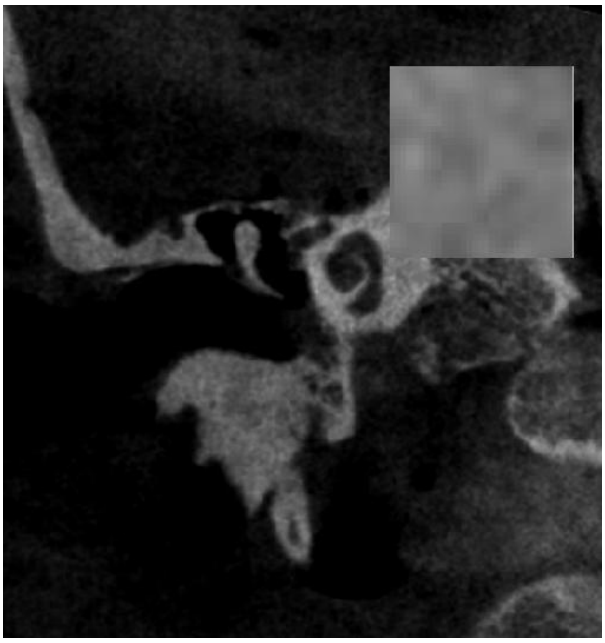

Figure 3.5: Raw image and cropped 30-by-30 pixels image used for standard deviation evaluation placed on the region of interest.

4. RESULTS

Following the procedure described in the material and methods chapter, the results of this work are divided into anatomical (visual) and noise (algorithm-based) analyses. The findings of the noise analysis carried out using the MATLAB algorithm were compared with the visual assessment findings. Both sets of findings were similar. The effect of the filter changes and the differences reported when the datasets for the three filter types were compared showed that Cu-Al filtration with a total filtration of 4.01 mm gives the best image quality and also a lower noise/error value. Additionally, increasing the number of projections to 150% generated images with better visual quality and a lower noise level when compared with images acquired at 100% projections. Finally, changing the tube current did not have a clear effect on the image quality when the images were visually assessed. However, the error differences between the two tube currents were more noticeable in the noise analysis.

4.1 Visual assessment results

Tables 4.1, 4.2, and 4.3 present the averages of the two visual assessment sessions carried out based on the following ranking: (0) absent, (1) hazey, (2) sharp, and (3) very sharp. During the visual assessments, images were inspected for changes in image quality due to changes in filtration, tube current, and number of projections based on the clarity of nine anatomical landmarks. The anatomical landmarks assessed were the following: tympanic membrane, incus, malleus and stapes, scutum, oval window, cochlea, vestibulum, semisircular canals, Eustachian tube, and the facial nerve canal.

4.1.1 Visual assessment results based on changing filtration.

Table 4.1 shows the effect of changes in filtration at 12.5 mA and 150% projections. On the vertical axis, each anatomical structure is displayed with its average rank when the three filter sets (displayed on top) were used. As shown in Table 4.1, the anatomical

landmarks were visible in all cases, but the image quality was best when Cu-Al filtration, 150% projection and 12.5 mA were used. A graphical representation of these values is presented in Figure 4.1.below.

Table 4.1: Average of the two visual assessments for the three filter combinations used (12.5 mA and 150% projections).

Anatomical Landmarks	Al-Al	Cu-Cu	Cu-Al
Tympanic Membrane	2	2	2
Incus, Malleus and Stapes	1.25	2	2.25
Scutum	1.5	2	2.25
Oval Window	1.5	2	3
Cochlea	1.5	2	2.5
Vestibulum	2	2	2.5
Semi-Circular Canals	1.5	2	2.5
Eustachian Tube	1.5	2	2
Facial Nerve Canal	1.75	2	2

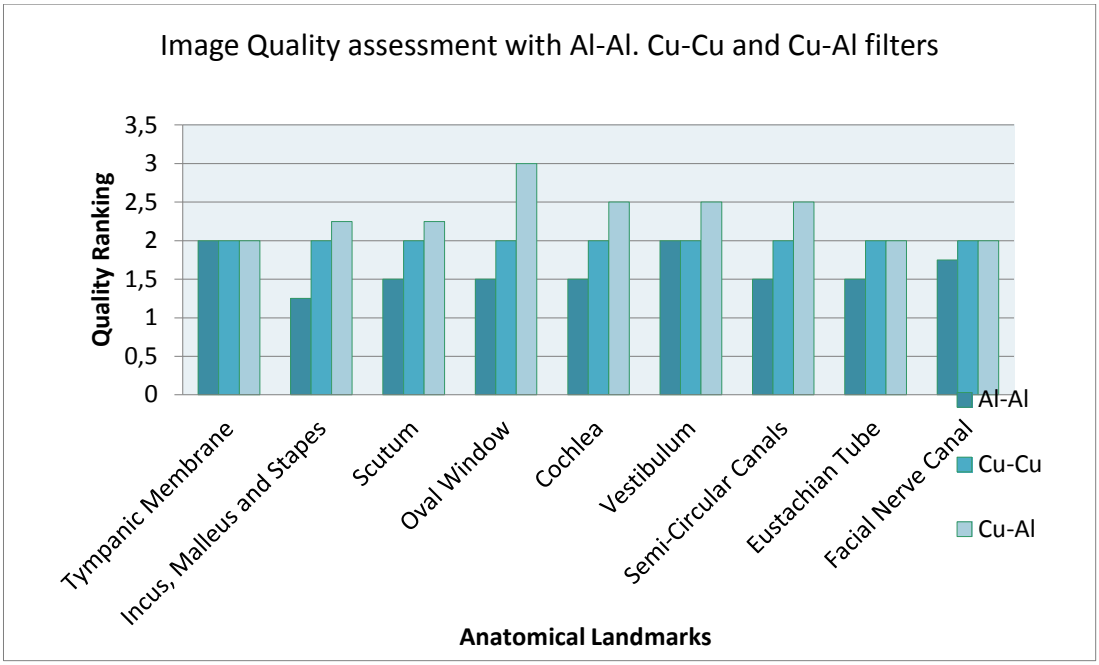

Figure 4.1: Bar chart showing the quality ranking (vertical axis) and the anatomical landmarks (horizontal axis) of the two visual assessments for the three filter combinations used.

4.1.2 Visual assessment results based on changing the tube current

Table 4.2 presents the effect of changes in tube current from 8 mA to 12.5 mA (100% projections and Cu-Cu filtration) on the image quality using (0) absent, (1) hazey, (2) sharp, and (3) very sharp as the ranking criteria. Surprisingly, the differences in image quality when tube current was changed from 8 mA to 12.5 mA were found to be minimal. Therefore, changes in tube current had only a very small effect on the image quality of the anatomical landmarks. However, when the number of projections was reduced to 100%, more information was obtained when 12.5 mA was used than when 8 mA was used.

Table 4.2: Average of the two visual assessments of 8 mA and 12.5 mA tube currents at 150% projections with Cu-Cu filters.

Anatomical Landmarks	8 mA	12 mA
Tympanic Membrane	1.5	2
Incus, Malleus and Stapes	2	2
Scutum	2	2
Oval Window	2	2
Cochlea	2	2
Vestibulum	2	2
Semi-Circular Canals	2	2
Eustachian Tube	2	2
Facial Nerve Canal	2	2

4.1.3 Visual assessment results based on changing the number of projections.

Table 4.3 presents the effects of changing the number of projections from 100% to 150% (12.5 mA and Cu-Cu filtration) on the image quality using (0) absent, (1) hazey, (2) sharp, and (3) very sharp as the ranking criteria. As can be seen from Table 4.3, when the number of projections was 150% the results were better than when 100% projections were used. This was because more projection or basis images were available for reconstruction at 150% projections and this affected the image quality. Figure 4.2 presents the average of the two visual assessments showing the effect of increasing the number of projections from 100% to 150% (12.5 mA and Cu-Cu filtration).

Table 4.3: Average of the two visual assessments showing the effect of increasing the number of projections from 100% to 150% (12.5 mA and Cu-Cu filtration)

Anatomical Landmarks	100% (number of projections)	150%(number of projections)
Tympanic Membrane	1.5	2
Incus, Malleus and Stapes	1	2
Scutum	1	2
Oval Window	1.25	2
Cochlea	1.75	2
Vestibulum	1	2
Semi-Circular Canals	1.75	2
Eustachian Tube	1.5	2
Facial Nerve Canal	1.5	2

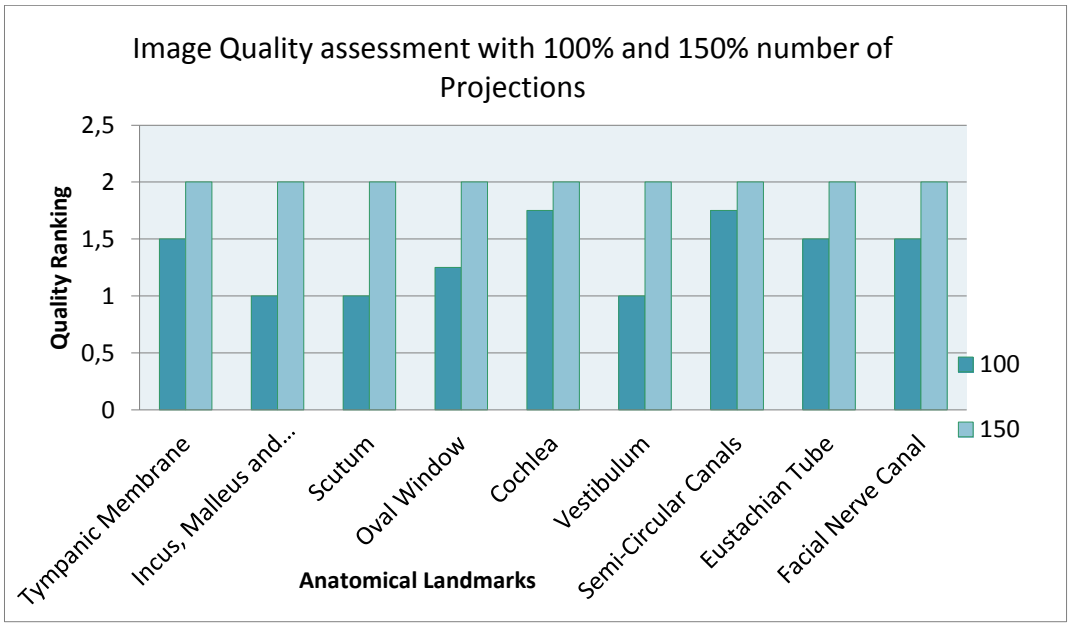

Figure 4.2: Average of the two visual assessments showing the effect of increasing the number of projections from 100% to 150% (12.5 mA and Cu-Cu filtration).

4.2 Noise analysis

Using the MATLAB algorithms (shown in Appendix 1), Table 4.4 shows the standard deviation values of the identical slices selected from the coronal data sets of the same images used in the visual assessment. The smallest standard deviation value shows the image with the best quality and the highest standard deviation value shows the image with the lowest quality.

Table 4.4: Exposure parameters and the filtration of the identical slices selected, and the standard deviation values obtained from the 30-by-30 ROI.

Exposure parameters used and filtration	Standard deviation
8 mA, 100% projection and Cu-Cu filtration	18.8236
12.5 mA, 100% projection and Al-Al filtration	12.8198
12.5 mA, 100% projection and Cu-Cu filtration	11.5809
8mA, 150% projections and Cu-Cu filtration	9.3944
12.5 mA, 150% projections and Cu-Cu filtration	9.0083
12.5mA, 150% projections and Al-Al filtration	8.5328
8mA, 150% projections and Cu-Al filtration	10.3694
12.5mA, 150% projections and Cu-Al filtration	8.0019

4.2.1 Noise analysis based on changing filtration

Figure 4.3 shows the standard deviation values obtained when the filtration was changed from Cu-Cu to Cu-Al and to Al-Al for a similar ROI (Figure 4.4) in three identical images. Figure 4.3 show that Cu-Al has the lowest standard deviation value. This implies that the coronal images obtained at 150% projections and 12.5 mA using

Cu-Al filtration have less noise when compared with the images obtained with the same parameters when Cu-Cu and Al-Al filtrations were used.

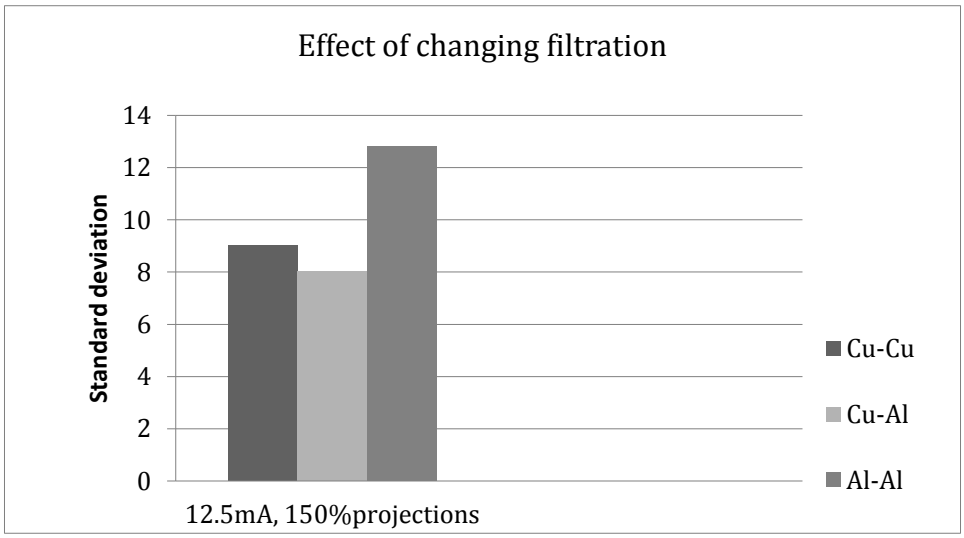

Figure 2.3: The bar chart of the plot of standard deviation values obtained when three different types of filtration were used at 150% projections and 12.5 mA.

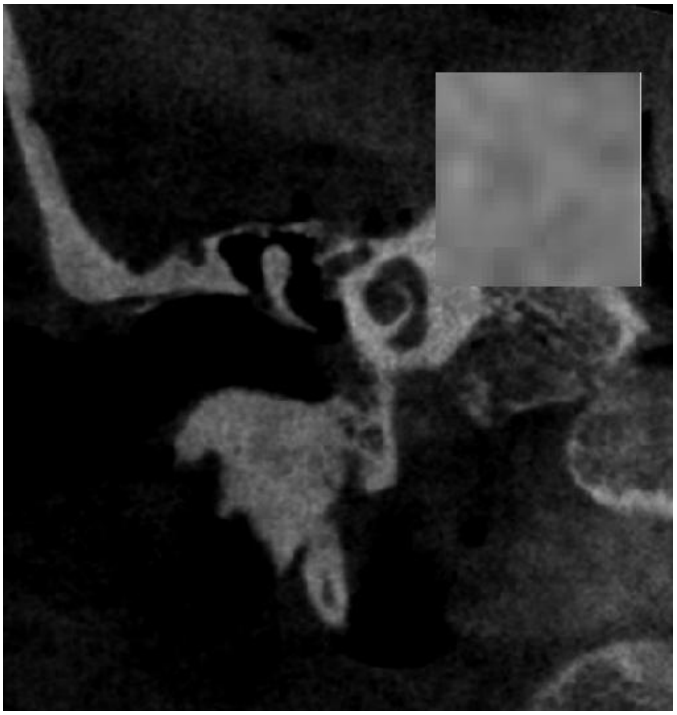

Figure 4.4: Coronal slice showing the entire image and the 30-by-30 ROI pixels used for evaluating the standard deviation.

4.2.2 Noise analysis based on changing the number of projections

Figure 4.5 shows the standard deviation values obtained when the number of projections was changed from 100% to 150% (Figure 4.6) in four identical images obtained when A-Al and Cu-Cu filtration was used. The standard deviation values obtained for 150% projections were lower than for Cu-Cu and Al-Al filtration. This shows that increasing the number of projections to 150% reduces the noise content of the images.

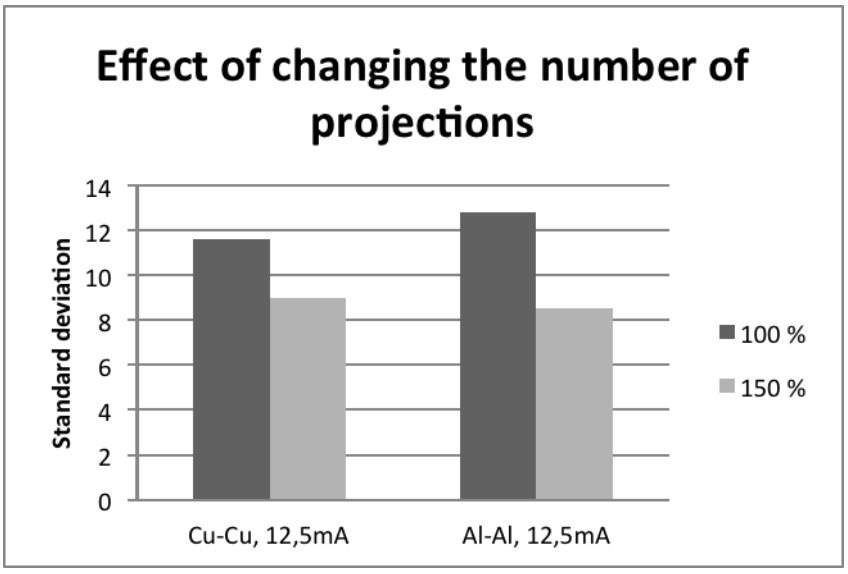

Figure 4.5: A plot of the standard deviation values obtained for 100% and 150% projections for Cu-Cu and Al-Al filtrations and 12.5 mA.

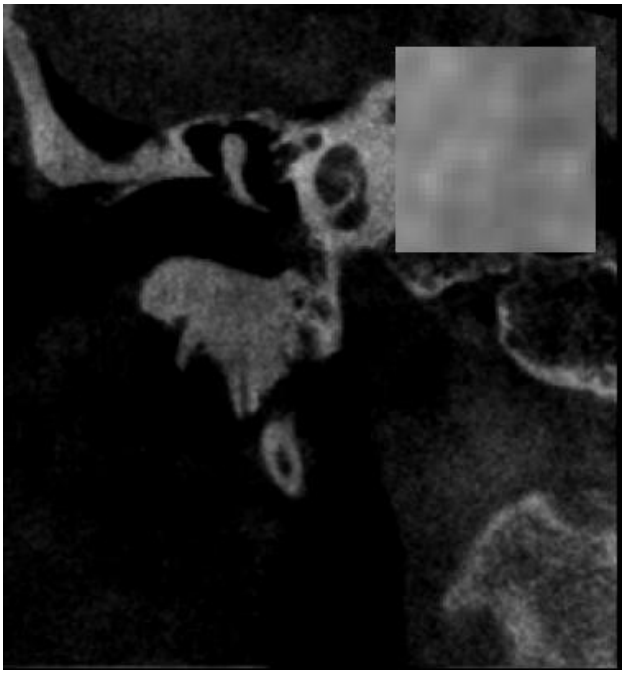

Figure 4.6: Coronal slice showing the entire image and the 30-by-30 ROI pixels used for evaluating the standard deviation.

4.2.3 Noise analysis based on changing the tube current

Figure 4.7 shows the standard deviation values obtained when the tube current was changed from 8 mA to 12.5 mA for a similar ROI (Figure 4.8) in four identical images selected when Cu-Al and Cu-Cu filtration were used. The standard deviation values obtained for 12.5 mA were lower when compared with the 8 mA values for both Cu-Al and Cu-Cu filtration. The changes were larger when Cu-Al filtration was used when compared with the values obtained when Cu-Cu filtration was used.

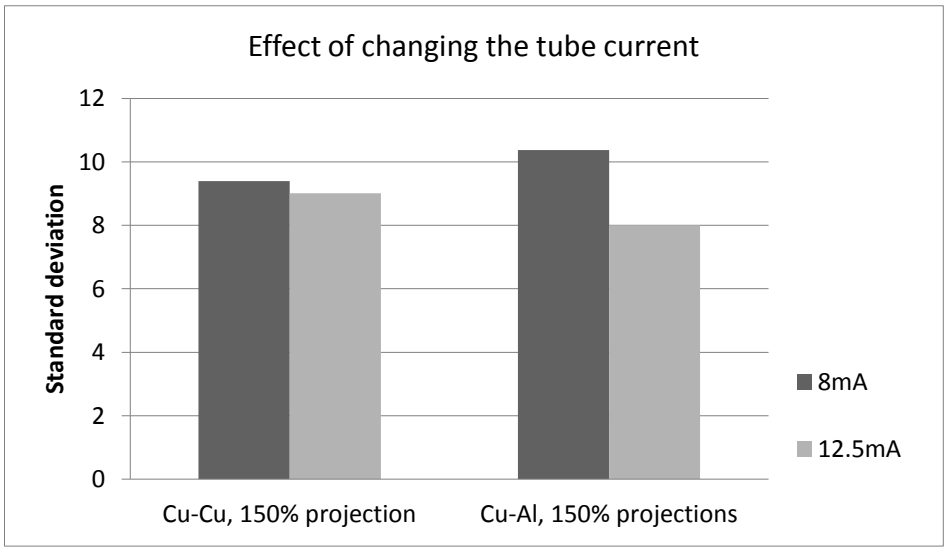

Figure 4.7: A plot of the standard deviation values obtained for 8 mA and 12.5 mA Cu-Cu and Cu-Al filtrations obtained at 150% projections.

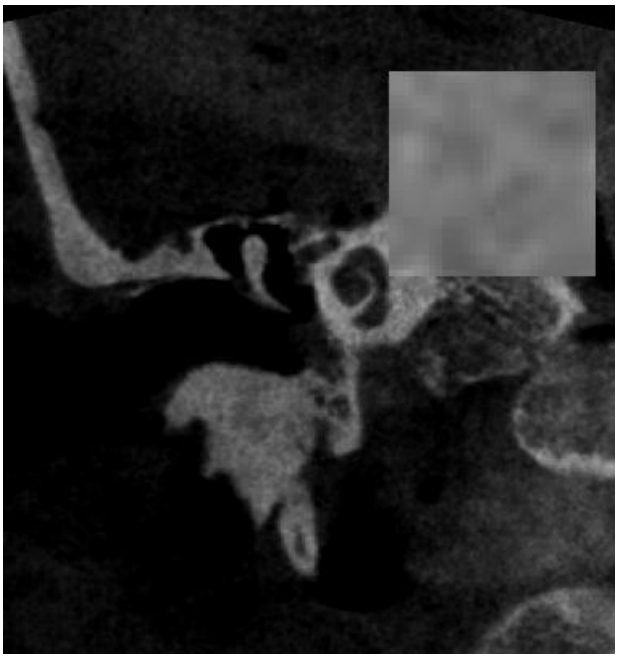

Figure 4.8: Coronal slice showing the entire image and the 30-by-30 ROI pixels used for evaluating the standard deviation.

5. DISCUSSION

This cadaver study comprised a temporal bone study and a sinus assessment study carried out on a Scanora 3D, cone-beam 3d imaging device. My part of the research focused on a comparative image quality assessment of CBCT temporal bone imaging based on filtration combination, X-ray tube current (milliamperage), and the number of projections used. Three filter sets: a 0.1 mm-0.1 mm Cu-Cu filter, a 3 mm-4 mm Al-Al filter, and a 0.1 mm-4 mm Cu-Al filter supplied and fitted by Soredex, Finland, were used in the image acquisition. Additionally, two tube currents of 8 mA and 12.5 mA, and a tube voltage of 90 kVp were used and the projection data were captured at standard 100% and 150% projections from a Scanora 3D, cone-beam 3d imaging system (Soredex, Tuusula, Finland).

The effectiveness of the filters, tube current, and projection increment were evaluated based on the image quality acquired from the temporal bone area. Conclusions were drawn based on the quality assessment results obtained by assessing the noise, and anatomical visibility of nine anatomical landmarks. The atomic number and the arrangement of the filters were found to have an effect on the quality of the images generated after the beam penetrated the object. Additionally, the images generated at 150% projections were of better diagnostic value and had a lower noise level when compared with those obtained at 100% projections in both the visual and algorithm-based assessment. However, the effect of the tube current changes from 8 mA to 12.5 mA was not so evident as they both gave similar image quality results. In summary, images generated with 4.1 mm filtration (copper and aluminum sandwich) at 12.5 mA and 150% projections produced the best image quality.

This study had several limitations. A major limitation was that a formalin-fixed cadaver head with an unknown medical history, removed brain, and no blood flow was used in the study. Unlike live patients, the cadaver head did not cause motion artifacts. Furthermore, being a formalin-fixed cadaver head, there might have been changes in the tissue properties. All these may have resulted in better image quality, changes in

attenuation of the tissues and, thus, the possibility of a wrong conclusion. In addition, the radiation doses were not measured during the imaging protocols.

5.1 The effect of using different filter sets

The results of the visual assessment and noise analysis showed that Cu-Al filtration at a thickness of 4.01 mm (equivalent to 7.3 mm Al) gave better image quality results when compared with both Al-Al filtration of 7 mm thickness and Cu-Cu of 0.2 mm (equivalent to 6.6 mm Al) thickness. The Cu-Cu filtration was second to Cu-Al filtration in the visual assessment while the Al-Al filtration was second in the noise analysis. This may be because the noise in the images did not prevent the observers from viewing the anatomical landmarks. However, the noise analysis calculated this noise without considering how much the noise interrupts the image visibility. Even though the aluminum equivalent thickness is about 7 mm in all the three filter sets, the effects were different. This was because copper is a higher atomic number material and attenuates low energy X-rays more than aluminum. However, high-energy photons, on the other hand, do not yield the best image quality in practice. As a result, it is necessary to effectively manipulate the material and combinations in order to generate the best image quality [25, 59: 9; 52].

This supports the results of Milton Costa et al. (2009) who in their results claimed that the interposition of aluminum and copper filters, especially when associated, results in improved image quality [9]. This further supports the results of Devito et al. (2006) where the contrasts of images were compared when Cu and Al filtration was used and concluded that a Cu filter produced better contrast images than an Al filter. [11]. Based on these results, and the explanations made by Joseph et al. [14], the filter material used has a more important role in beam filtration than the thickness of the filter material.

5.2 The effect of changing the tube current

From the visual assessment results obtained, tangible changes were not detected in the diagnostic values of all the images when the tube current was changed from 8 mA to 12.5 mA or vice versa. In a few cases, the 12.5 mA images were of a better quality. The results of the noise analysis showed that 12.5 mA had better image quality because the standard deviation values were lower than the standard deviation values obtained when 8 mA was used. The question of what is acceptable image quality and whether the noise interrupts the anatomical details depends on the observer. In addition, the tube current depends on the FOV [9], tube voltage (mAs), and the intensity (I) used. Hence, effective manipulation of these parameters in CBCT temporal bone imaging to create a good balance between the image quality and the As Low As Reasonably Achievable (ALARA) principle is necessary.

The findings of this thesis is supported by the results of Jeffrey et al. (2007) and Sohaib et al. (2001) [23; 54] who both concluded that no significant image quality difference occurred when the mA is changed. In an earlier study by Palomo et al. (2006), however, reduced image quality was reported. The reason why **t**his observation was not found in our study may be because a cadaver head was studied and not C-Phantoms [41] as was the case in their earlier study.

5.3 The effect of varying the number of projections

The results of the visual assessment and noise analysis showed that the image quality in all cases when 150% projections were used possesses less noise and clearer anatomical details when compared with the quality at 100% projections. However, the anatomical details obtained when the number of projections was 100% were also found to be good, but cannot be compared with the quality of the anatomical details produced when the number of projections was increased to 150%.

This supports the claims of Sakata et al. (2007) who investigated the Optimization of TACT imaging protocols for the in situ visualization of cochlear electrode arrays in feline temporal bones. They found that the quality of the resulting images, evaluated as a function of image contrast, improved with the larger number of basis images that

resulted from increasing the number of projection [50]. The question of what is acceptable image quality and what is an important anatomical landmark are important questions. Bo Lu et al. (2010) claim that reducing the number of projections allows a good balance between dose reduction and contrast visibility. Furthermore, their results showed that increasing the number of projections increases the scanning time and does not significantly influence detailed contrast visibility as the images obtained at a lower number of projections are also diagnostically acceptable [33]. This observation was also found in our study. However, the complexity of the temporal bone may require an increased number of projections in order to effectively characterize the entire anatomy. Moreover, Bo Lu et al. study was based on Image Guidance for Radiotherapy (IGRT) and this method requires that the patient dose produced by image acquisition should be as low as possible because the scanning times used in this method are much longer.

5.4 Reliability of the results

In the visual assessment, all the slices of coronal, sagittal and axial images were used in the evaluation. In the noise analysis, however, only eight identical images were selected from the coronal dataset for the evaluation.

The standard deviation values used in the noise assessment were successful because the cadaver head used in this study was fixed and the images acquired in each case were identical. In real patients, motion artifacts may cause changes in the images acquired from the same location. For this reason, this method may not be effective for noise assessment in clinical applications [21; 26; 39].

The visual assessments were reliable as they are used for medical image analysis in practice. In this study, the views of the two radiologists with over 20 years' experience in the field of radiology were employed. Additionally, the cadaver head model used in this study mimics the real patient and may be preferred to a phantom model because it possesses the skin and temporal bone features whose properties affects the image quality. The cadaver model attenuated the photons in a similar manner, as would have been the case when real patients were used. However, assessing real patients may give a better result and this has been listed in the limitations of this thesis. Furthermore, only

one cadaver head was used in this study. A larger study with more than one cadaver head or real patients with varying size, bone age, and sex may provide more information in the image analysis.

Finally, ten scanning protocols with no enhancement or windowing were acquired and used in this study. No scanning was done with Cu-Al filtration at 100% projections. For this reason, no comparative analysis was carried out at 100% projections when Cu-Al filtration was used.

6. CONCLUSION

In this thesis, a comparative image quality assessment of CBCT temporal bone imaging based on filtration combination, X-ray tube current (milliamperage), and the number of CBCT-projections was carried out. Copper and Aluminum (Cu-Al) filters offered the best image quality when compared with the factory-fitted Cu-Cu and Al-Al filter combinations in both anatomical clarity assessments and noise analyses. From the results, it was also demonstrated that increasing the number of projections from the standard 100% number of projections to 150% offered a better characterization of the complex temporal bone anatomy. Finally, changing the tube current from 8 mA to 12.5 mA resulted in a minimal change in the image quality when visually assessed. However, the effect of the tube current variations increased when the noise analyses were carried out.

In conclusion, variations in the material property of the filter, effective filter inter-positioning and variations in the number of projections optimized the image quality in CBCT temporal bone imaging

This study has several limitations. A major limitation was that a formalin-fixed cadaver head with an unknown medical history, removed brain, and no blood flow was used in the study. Unlike normal patients, the cadaver head did not cause motion artifacts. Furthermore, being a formalin-fixed cadaver head, there might have been changes in the tissue properties. This may have resulted in better image quality, changes in the attenuation of tissues, and, thus, the possibility of the misleading results. In addition, the radiation doses were not measured during the imaging protocols.

Because CBCT has become more popular for temporal bone imaging, the results of this study underline the need for further investigations into the effects of exposure parameters and filtration by using filters made from other materials other than the standard Cu and Al. A further study based on the evaluation of changes, in terms of image quality, resulting from the use of different filter shapes could also be carried out.

In addition, a similar study of the sinus area, another area where CBCT has become popular, using the same parameters could be carried out to demonstrate the tissue characterization in support of the findings of this thesis. Furthermore, a real patient study with diseased patients and control patients with no temporal bone defects using the same parameters could further clarify and strengthen the findings of this thesis. Finally, the effect of these filter combinations may also be tested in the dentomaxillofacial imaging encountered in dental-implant planning, the treatment of craniofacial fractures, and orthodontics in order to evaluate their overall efficiencies.

APPENDICES

Appendix 1

The MATLAB algorithm used for the noise analysis in calculating standard deviation is presented below. The heading of each algorithm describes the evaluation in each case and each loaded image is named in relation to the exposure parameters and the filtration used [6; 46].

```
%Standard deviation calculation for the slice from 12.5mA, 100%
projections and Cu-Cu filtration
clear all
close all
clc
%loading of image
I1=imread('0.1mm0.1mm12,5mAcor.jpg');
%image before cropping
figure; imshow(I1,[])
%cropping the image to localize region of interest (ROI)
IC1=imcrop(I1,[564 259 30 30]);
%image after cropping
figure; imshow(IC1,[])
%calculating the standard deviation
s=std(double(IC1(:)));
```

```
%Standard deviation calculation for the slice from 8mA, 150%
projections and Cu-Cu filtration
clear all
close all
clc
%loading of image
I2=imread('0.1mm0.1mm8mAcor.jpg');
%image before cropping
figure; imshow(I2,[])
%cropping the image to localize region of interest (ROI)
IC2=imcrop(I2,[504 348 30 30]);
%image after cropping
figure; imshow(IC2,[])
%calculating the standard deviation
s=std(double(IC2(:)));
```

```
%Standard deviation calculation for the slice from 12,5mA, 150%
projections and Cu-Cu filtration
clear all
close all
clc
```

```
%loading of image
I3=imread('50%0.1mm0.1mm12,5mAcor.jpg');
%image before cropping
figure; imshow(I3,[])
%cropping the image to localize region of interest (ROI)
IC3=imcrop(3,[506 351 30 30]);
%image after cropping
figure; imshow(IC3,[])
%calculating the standard deviation
s=std(double(IC3(:)));
```

```
%Standard deviation calculation for the slice from 12,5mA, 100%
projections and Al-Al filtration
clear all
close all
clc
%loading of image
I4=imread('0.1mm0.1mm8mAcor.jpg');
%image before cropping
figure; imshow(I4,[])
%cropping the image to localize region of interest (ROI)
IC2=imcrop(I4,[558 330 30 30]);
%image after cropping
figure; imshow(IC4,[])
%calculating the standard deviation
s=std(double(IC4(:)));
```

```
%Standard deviation calculation for the slice from 12,5mA, 150%
projections and Al-Al filtration
clear all
close all
clc
%loading of image
I5=imread('50%4mm3mm12,5mAcor.jpg');
%image before cropping
figure; imshow(I5,[])
%cropping the image to localize region of interest (ROI)
IC1=imcrop(I5,[577 379 30 30]);
%image after cropping
figure; imshow(IC5,[])
%calculating the standard deviation
s=std(double(IC5(:)));
```

```
%Standard deviation calculation for the slice from 12,5mA, 150%
projections and Cu-Al filtration
clear all
close all
clc
%loading of image
I6=imread('50%0.1mm4mm8mAcor.jpg');
%image before cropping
figure; imshow(I6,[])
%cropping the image to localize region of interest (ROI)
IC6=imcrop(I1,[587 286 30 30]);
%image after cropping
```

```
figure; imshow(IC6,[])
%calculating the standard deviation
s=std(double(IC6(:)));


%Standard deviation calculation for the slice from 12,5mA, 150%
projections and Cu-Al filtration
clear all
close all
clc
%loading of image
I7=imread('50%0.1mm4mm12,5mAcor.jpg');
%image before cropping
figure; imshow(I7,[])
%cropping the image to localize region of interest (ROI)
IC7=imcrop(I7,[577 286 30 30]);
%image after cropping
figure; imshow(IC7,[])
%calculating the standard deviation
s=std(double(IC7(:)));
```

REFERENCES

[1] Barrett J. and Keat N., Artifacts in CT: recognition and avoidance, The journal of continuing medical education in Radiology, (2004), RadioGraphics, 24, 1679-1691pp.

[2] Behrman, Richard H., Study guide to computed tomography advanced applications (1994). Greenwich, Connecticut: Clinical Communications Inc.

[3] Benjamin C. W. and William C. S., Hearing and Balance Anatomy, [electronic journal], [accessed on 12.06.2011], available at: http://www.medicinenet.com/script/main/art.asp?articlekey=21685

[4] Buades A., Coll B., and Morel, A review of image denoising algorithms, with a new one, Society for industrial and applied mathematics (2005) Vol. 4, No. 2, pp. 490–530.
Bushberg, Jerrold T., Seibert, J. Anthony, Leidholdt, Edwin M. and Boone, John M. (1994), The Essential Physics of Medical Imaging. St. Baltimore: Williams & Wilkins.

[5] Chakeres D. W., Augustyn M. A., Temporal bone: Imaging [electronic journal], [accessed on 17.18.2011]. Available at http://www.similima.com/books/radiologybooks/radiologybook4.pdf

[6] Chen T., Chuang K., A new image compression method using noise bit removal, International congress series on computed assisted radiology and surgery, Volume 1230, June 2001, Pages 773-778.

[7] Cohnen M., Fischer H., Hamacher J., Lins E., Kotter R., and Modder U., CT of the head by use of reduced current and kilovoltage: Relationship between image quality and dose reduction, AJNR Am J Neuroradiol 21:1654–1660, October 2000.

[8] Cone Beam 3D and digital panoramic imaging combined in one system, Scanora 3D Bronchure, Soredex Tuusula, Finland, 2011.

[9] Costa M. M. B., Leocadio da Nova J. L., and Canevaro L. V., Effect of additional filtration on radiation doses and image quality in videofluoroscopic studies, Radiol Bras vol.42 no.6 São Paulo Nov./Dec. 2009.

[10] Dalchow C. V., Weber A. L., Yanagihara N., Bien S., Werner J. A. Digital volume tomography: Radiologic examinations of the temporal bone. America Journal of Roentgenology 2006; 186: 416-23pp.

[11] Devito K. L., Rubira M. J., Tamburus J. R., Lavrado M. A. S., Copper filter for dental radiology: evaluation of radiographic contrast, Rev. Ciênc. Méd., Campinas, 15(2006):487-493.

[12] Ejere D., Optimization of cone-beam CT image quality for image guided radiotherapy, Master's Thesis, Amsterdam, 2006, Academic Medical Center, University of Amsterdam, Netherlands, 91p.

[13] Ernest E. Charlton, "X-ray tube," in AccessScience, ©McGraw-Hill Companies, 2008, http://www.accessscience.com

[14] Faccioli N., Barillari, M., Guariglia S., Zivelonghi E., Rizzotti A., Cerini R., Pozzi Mucelli R., Radiation dose saving through the use of cone-beam CT in hearing-impaired patients, Radiol. Med (2009) 114: 1308-1318.

[15] Fatterpekar G. M., Doshi A., Delman B. N., 3D CT of the Temporal bone: Anatomy and Pathology, Department of Radiology, Mount Sinai Medical Center, New York 2006, USA.

[16] Güldner C., Wiegand S., Weiß R., Bien S., Sesterhenn A., Teymoortash A., Diogo I., Artifacts of the electrode in cochlea implantation and limits in analysis of deep insertion in cone beam tomography (CBT), 2011 Eur

Arch Otorhinolaryngol DOI 10.1007/s00405-011-1719-3, [electronic journal], [accessed on 18. 08.2011].

[17] Hanso K. M., Noise and contrast discrimination in computed tomography, In: T. H. Newton and D. G. Potts, Radiology of the skull and brain, Technical Aspects of Computed Tomography, Vol. 5, St. Louis, USA, 1981. Available at http://kmh-lanl.hansonhub.com/publications/rsb81.pdf

[18] Hawkins J. E., Britannica Encyclopedia Online- Human ear: In Encyclopedia Britannica Corporate site 2011 [electronic Journal], accessed on June 12, 2011, available at http://www.britannica.com/EBchecked/topic/175622/human-ear

[19] Hendee W. R., Ritenour E. R., Medical imaging physics 4th edition, New York , USA 2002, Willey-Liss, Inc., Publication. 512pp.

[20] Heurich T., Ziegler C., Steveling H., Wörtche R., Mühling J., Hassfeld S. Digital volume tomography-an extension to the diagnostic procedures available for application before surgical removal of third molars. Mund Kiefer Gesichtschir 2002, 6:427-432pp.

[21] Hodez C., Griffaton-Taillandier C., Bensimon I., Cone-beam imaging: Applications in ENT, European Annals of Otorhinolaryngology, Head and Neck diseases (2011) 128, 65-78.

[22] IAEA Training material on radiation protection in diagnostic and interventional radiology: Radiation protection in diagnostic and interventional radiology. Indications and techniques for ear and petrous temporal bone imaging 2008, sponsor by French society of oto-rhino-laryngology head and neck surgery; represented by the Association Française d'Otologie et d'Otoneurologie (AFON) [electronic journal], [accessed on 19/08/2011].

[23] Jeffrey C. K., Palomo J. M., Landers M. A, Figueroa A., and Mark G. H., Image quality produced by different cone-beam computed tomography

settings, American Association of Orthodontists, doi:10.1016/j.ajodo.2007.02.053.

[24] John B. L. and Ivanovic M., Comparative dosimetry of dental CBCT devices and 64-slice CT for oral and maxillofacial radiology, Oral surgery, Oral Medicine, Oral Pathology, Oral Radiology, oral Endodontology 2008;106:106-14).

[25] Joseph N., Phalen J., CE essesntials, Online Radiography Continuing Education for Radiologic X ray Technologist, Part 4 principles of radiation protection and ALARA [electronic journal], [accessed on 25.08.2011], available at: http://www.ceessentials.net/article5.html#section4_1

[26] Karhuketo T.S., Dastidar P.S., Laasonen E. M., Sipila M.M., Puhakka H.J., Visualization of the middle ear with high resolution computed tomography and superfine fiberoptic videomicroendoscopy, EurArchtorhinolaryngol. 1998; 255(6):277-80.

[27] Ketcham, R. A. and Carlson, W. D., Acquisition, optimization and interpretation of X-ray computed tomographic imagery: Applications to the geosciences. Computers & Geosciences 27 (2001) 381–400.

[28] Kiljunen T., Patient doses in ct, dental cone beam ct and projection radiography in Finland, with emphasis on paediatric patients, Radiation and Nuclear Safety Authority STUK Department of Physics, Faculty of Science, University of Helsinki, 2008.

[29] Koedooder K. and Venema H. W., Filter materials for dose reduction in screen-film radiography, Phys. Med. Biol., 1986, Vol. 31, No 6, 585-600pp.

[30] Lee R. D., Common image artifacts in cone beam CT. Oral and Maxillofacial Radiology, The Summer 2008 AADMRT Newsletter, University of Texas Health Science Center San Antonio, TX.

[31] Lemmerling M. M., De Foer B., Verbist B. M.and VandeVyver V., Imaging of Inflammatory and Infectious Diseases in the Temporal Bone, Neuroimaging Clinics of North America, Volume 19, Issue 3, August 2009, 321-337pp.

[32] Li T. and Xing L., Optimizing 4D Cone-Beam Acquisitio protocol for external beam radiotherapy, International Journal on Radiation Oncology Biol. Phys. (2007), Vol. 67, No. 4, pp. 1211–1219pp.

[33] Lu B., Lu H. and Palta J., A comprehensive study on decreasing the kilovoltage cone-beam CT dose by reducing the projection number, Journal of Applied Clinical Medical Physics, Vol 11, No 3 (2010).

[34] Lu D., Bai E., Wang G., Computed tomography In: Akay M. Wiley Encyclopedia of Biomedical Engineering, Vol. Inc., Publication, 4056pp.

[35] Mass, weight, density or specific gravity of different metals, [electronic journal], [accessed on 16.08.2011], available at http://www.simetric.co.uk/si_metals.htm

[36] McNitt-Gray M. F., Geffen D., Tradeoffs in CT image quality and dose [electronic journal], [accessed on 20.07.2011]. Available at: http://www.oucom.ohiou.edu/oumicroct/Downloads/Tradeoffs_in_CT_Image_Quality_and_Dose_9794-13379.pdf

[37] Micheau A., and Hoa D., Anatomy of the petrous bone (CT). In; Atlas of human anatomy using cross-sectional imaging, Imaios, SAS, 2008, Available at: http://www.imaios.com/en/e-Anatomy/Head-and-Neck/Petrous-bone-CT

[38] Miracle A. C. and Mukherji S. K., Conebeam CT of the Head and Neck, Part 2: Clinical Application, American Journal of Neuroradiology (2009) 30:1285-1292pp.

[39] Miracle A. C. and Mukherji S. K., Conebeam CT of the head and neck, part 1: clinical application, American Journal of Neuroradiology (2009) 30:1285-1292pp.

[40] Mueller K., Yagel R., and Wheller J. J., "Fast implementations of algebraic methods for the 3D reconstruction from cone-beam data," IEEE Transactions on Medical Imaging, vol. 18, no. 6, pp. 538-547, 1999.

[41] Palomo J. M., Subramanyan K., Hans M., Influence of mA settings and a copper filter in CBCT image resolution, Intertational Journal on Computed Assisted Radiology and Surgery 2006 1:391-3pp.

[42] Pauwels R., Beinsberger J., Collaert B., Theodorakou C., Rogers J., Walker A., Cockmartin L., Bosmans H., Jacobs R., Bogaerts R., Horner K., Effective dose range for dental cone beam computed tomography scanners, European Journal of Radiology (2011), doi:10.1016/j.ejrad.2010.11.028

[43] Peltonen L. I., Aarnisalo A. A., Kortesniemi M. K., et al. Limited cone-beam computed tomography imaging of the middle ear: a comparison with multislice helical computed tomography. Acta Radiol 2007; 48:207–1pp.

[44] Peltonen L., Novel surgical and imaging methods of the middle ear and temporal bone, Doctoral dissertation, Helsinki, 2008, University of Helsinki, Faculty of Medicine, Institute of Clinical Medicine, Department of Otorhinolaryngology, Helsinki, Finland.

[45] Ponomarenko N., Lukin V., Egiazarian K., Astola J., Carli M. and Battisti F., Color image database for evaluation of image quality metrics, [electronic journal], [accessed on 30.08.2011], available at: http://www.comlab.uniroma3.it/Marco/Articoli%20Battisti/Color%20Image%20Database%20for%20Evaluation%20of%20Image%20Quality%20Metrics.pdf.

[46] R2011b documentation-MATLAB, Mathworks, 3 Apple Hill Drive, Natick, MA 01760-2098, United States.

[47] Raparia D., Alessi J., and Kponou A., The algebraic reconstruction technique (ART), AGS Department, Brookhaven National Lab, Upton, NY 11973, USA, [electronic journal], [accessed on 25.08.2011], available at http://epaper.kek.jp/pac97/papers/pdf/2P057.PDF

[48] Reddinger W., CT Image Quality, OutSource, Inc, 1998, available at http://www.e-radiography.net/mrict/CT_IQ.pdf
Robinson T., Using Electron Bean Computed Tomography (EBCT) to Assess Pulmonary Function in Patients with Cystic Fibrosis. 1997. Available at: http://www.cfri.org/news/97spring/res197sp.html

[49] Romans L., CT image quality [www], [accessed on 20.07.2011]. Enterprises for Continuing Education Inc. (ECEI), PO Box 300, Brighton, MI 48116, (810) 229-3354, available at http://www.cewebsource.com/coursePDFs/CTimageQuality.pdf

[50] Sakata M., Hareyama M., Heil T. A., Henson M. M., Henson O. W. Jr, Nair M. K., Smith D. W., Optimization of TACT imaging protocols for in situ visualization of cochlear electrode arrays in cat temporal bones, Ear Hear. 2007 Aug; 28(4):444-50.

[51] Scarfe W. C., Farman A. G., What is cone-beam CT and how does it work? The Dental Clinic of North America 52 (2008) 707–730pp.

[52] Seibert J. A., Boone J. M., X-Ray imaging physics for nuclear medicine technologists. Part 2: X-ray interactions and image formation, Journal of Nuclear medicine technology, March 1, 2005 vol. 33 no. 1: 3-18.

[53] Seshadrinathan K., Thrasyvoulos N. P, Robert J. S., Junqing C., Zhou W., Hamid R. S, and Alan C. B., Image quality assessment, [electronic journal], [accessed on 28.08.2011], available at://www.download-

it.org/free_files/Pages%20from%20Chapter%2021-a083d09ec93486e5de61a062d13060cb.pdf

[54] Sohaib S. A., Peppercorn P. D., Horrocks J. A., Keene M. H., Kenyon G. S., Reznek R. H., The effect of decreasing mAs on image quality and patient dose in sinus CT, Br J Radiol. 2001 Feb;74(878):157-61

[55] Suomalainen A., Cone-beam computed tomography in oral radiology, Doctoral dissertation, Helsinki, 2010, Department of Radiology, Helsinki University Central Hospital, Finland, 80p.

[56] Swartz J. D., Harnsberger; Imaging of the temporal bone 3rd edition, New York, USA 1998, Thieme Medical Publishers, Inc., 479pp.

[57] Swartz J. D., Loevner L. A., Imaging of the temporal bone, 4th edition, New York, USA 2009, Thieme Medical Publishers, Inc., 592pp.

[58] Tantanapornkul W., Okouchi K., Fujiwara Y., Yamashiro M., Maruoka Y., Ohbayashi N., Kurabayashi T.: A comparative study of cone-beam computed tomography and conventional panoramic radiography in assessing the topographic relationship between the mandibular canal and impacted third molars. Oral Surg Oral Med Oral Pathol Oral Radiol Endod 103:253-259, 2007.

[59] Trout D. E., Kelly J. P. and Cathey G. A. The use of filters to control radiation exposure to the patient in diagnostic roentgenology, Am J Roentgenol Radium Ther Nucl Med. 1952; 67(1):946-62.

[60] Tyndall D. A., Rathore S., Cone-beam CT diagnostic applications: caries, periodontal bone assessment, and endodontic applications, Dental Clinics of North America, Volume 52, Issue 4, October 2008, 825-8pp.

[61] U.S. Department of Health and Human Services, Food and Drug Administration, Center for Devices and Radiological Health, Diagnostic

Devices Branch, Division of Mammography Quality and Radiation Programs, Office of Communication, Education, and Radiation Programs, Provision for alternate measure of the computed tomography dose index (CTDI) to assure compliance with the dose information requirements of the federal performance standard for computed tomography, 2006 [electronic journal], [accessed on 01.07.2011]. Available at: http://www.fda.gov/MedicalDevices/DeviceRegulationandGuidance/GuidanceDocuments/ucm094379.htm

[62] Williams P. L., Warwick R., Dyson M., Bannister L. H., Gray's anatomy 37th Edition, New York 1989: 1219–43pp.

[63] Workman A., Brettle D. S. Physical performance measures of radiographic imaging systems. Dentomaxillofacial Radiol, 1997 pages 139-146.

[64] Workshop on dental Cone Beam CT, SEDENTEXCT, Dosimetry of dental CBCT, 2011. Available at http://www.sedentexct.eu/system/files/Prof.%20Bogaerts.pdf

[65] Zhan Y., Zhang L., Zhu X. R., Lee A., Chambers M. and Dong L., Reducing metal artifacts in cone- beam CT image preprocessing projection data. Int. J. Radiation Oncology Biol. Phys. (2007), Vol. 67, No. 3, pp. 924–932pp.

[66] Zhao X., Hu J. and Zhang P.: GPU-Based 3D cone-beam CT image reconstruction for large data volume, International Journal of Biomedical Imaging, Volume 2009 (2009), Article ID 149079, 8pp.